**Showcasing research from Prof. Karabencheva-Christova's laboratory, Department of Chemistry, Michigan Technological University, MI, USA.**

Unusual catalytic strategy by non-heme Fe(II)/2-oxoglutarate-dependent aspartyl hydroxylase AspH

Our study illuminates the origin of the atypical catalytic strategy employed by the human non-heme Fe(II)/2-oxoglutarate-dependent dioxygenase AspH. We emphasize the pivotal role played by a water molecule, stabilized by a second coordination sphere aspartate residue, in catalysis, replacing the conventional iron-coordinated carboxylate ligand.

Image credits: Sarah Atkinson, Anandhu Krishnan, and Tatyana Karabencheva-Christova. Background image by Jezper, Okea, and Sveta – stock.adobe.com

## As featured in:

ROYAL SOCIETY OF CHEMISTRY

rsc.li/chemical-science

# Unusual catalytic strategy by non-heme Fe(II)/2-oxoglutarate-dependent aspartyl hydroxylase AspH†

Anandhu Krishnan, [a] Sodiq O. Waheed, [a] Ann Varghese,[a] Fathima Hameed Cherilakkudy,[a] Christopher J. Schofield [b] and Tatyana G. Karabencheva-Christova [*a]

Biocatalytic C–H oxidation reactions are of important synthetic utility, provide a sustainable route for selective synthesis of important organic molecules, and are an integral part of fundamental cell processes. The multidomain non-heme Fe(II)/2-oxoglutarate (2OG) dependent oxygenase AspH catalyzes stereoselective (3*R*)-hydroxylation of aspartyl- and asparaginyl-residues. Unusually, compared to other 2OG hydroxylases, crystallography has shown that AspH lacks the carboxylate residue of the characteristic two-His-one-Asp/Glu Fe-binding triad. Instead, AspH has a water molecule that coordinates Fe(II) in the coordination position usually occupied by the Asp/Glu carboxylate. Molecular dynamics (MD) and quantum mechanics/molecular mechanics (QM/MM) studies reveal that the iron coordinating water is stabilized by hydrogen bonding with a second coordination sphere (SCS) carboxylate residue Asp721, an arrangement that helps maintain the six coordinated Fe(II) distorted octahedral coordination geometry and enable catalysis. AspH catalysis follows a dioxygen activation-hydrogen atom transfer (HAT)-rebound hydroxylation mechanism, unusually exhibiting higher activation energy for rebound hydroxylation than for HAT, indicating that the rebound step may be rate-limiting. The HAT step, along with substrate positioning modulated by the non-covalent interactions with SCS residues (Arg688, Arg686, Lys666, Asp721, and Gln664), are essential in determining stereoselectivity, which likely proceeds with retention of configuration. The tetratricopeptide repeat (TPR) domain of AspH influences substrate binding and manifests dynamic motions during catalysis, an observation of interest with respect to other 2OG oxygenases with TPR domains. The results provide unique insights into how non-heme Fe(II) oxygenases can effectively catalyze stereoselective hydroxylation using only two enzyme-derived Fe-ligating residues, potentially guiding enzyme engineering for stereoselective biocatalysis, thus advancing the development of non-heme Fe(II) based biomimetic C–H oxidation catalysts, and supporting the proposal that the 2OG oxygenase superfamily may be larger than once perceived.

*aDepartment of Chemistry, Michigan Technological University, Houghton, MI 49931, USA. E-mail: tatyanak@mtu.edu*

*bChemistry Research Laboratory, Department of Chemistry and the Ineos Oxford Institute for Antimicrobial Research, University of Oxford, OX1 3TA, Oxford, UK*

† Electronic supplementary information (ESI) available. See DOI: https://doi.org/10.1039/d3sc05974j

## Introduction

Enzyme-catalyzed hydroxylation of C–H bonds of proteins is a post-translational modification that in animals is involved in many important processes.[1] Hydroxylation of specific proline- and lysine-residues in procollagen, for example, as catalyzed by prolyl- and lysine-hydroxylases is essential for the function and stability of collagen, the most abundant protein in metazoans.[2,3] Hydroxylated amino acid residues are present in numerous biologically active natural products,[4–7] and such hydroxylations provide valuable starting points for further chemical modifications.[8] Hydroxylations of aspartyl and asparaginyl residues, as catalyzed by the aspartate/asparagine-β-hydroxylase (AspH) and factor-inhibiting hypoxia-inducing factor (FIH), are proposed to play crucial roles in regulating hypoxia,[9,10] calcium signaling,[11,12] and blood coagulation.[13–15] AspH catalyzes the post-translational C3 hydroxylation of specific aspartate and asparagine residues in the epidermal growth factor-like domains (EGFDs), which perform vital biological functions,[16,17] including intercellular signaling,[18–21] calcium binding,[22–25] and extracellular matrix formation.[26–28]

Direct and selective functionalization of C–H bonds is an efficient and powerful tool for synthesizing complex molecules.[29–31] However, achieving regio- and stereoselective C–H bond oxidation poses significant challenges due to the

high bond dissociation energy and the presence of multiple C–H bonds within the molecules.[32,33] Consequently, the pursuit of environmentally friendly and cost-effective synthetic methods for C–H oxidation reactions has gained substantial attention.[34–36] Enzymes provide a sustainable solution, as both natural and engineered enzymes selectively and efficiently mediate diverse C–H oxidation reactions.[37–43] Notably, heme- and non-heme iron-containing enzymes catalyze direct C–H oxidations with remarkable stereo- and regio-selectivity[8,39,44,45] thus offering valuable insights for applying redesigned enzymes as synthetic utilities.[46–49] In contrast to small molecule catalysts, enzymes can be continuously optimized, redesigned and repurposed for performing specific C–H reactions with industrial importance.[50–52] Residues in the Second Coordination Sphere (SCS) and Remote Areas (RA) became increasingly important tools for modulating and improving enzyme activity and product selectivity.[53–59]

Non-heme Fe(II) and 2-oxoglutarate (2OG) dependent oxygenases are gaining prominence as industrial biocatalysts, owing to their scalability and versatility.[60] AspH (Fig. 1) is a non-heme Fe(II)/2OG hydroxylase, that catalyzes the stereoselective (3$R$)-hydroxylation of aspartyl- and asparaginyl-residues in EGFDs.[15,61–64] AspH is essential for normal human biology and has assigned roles in placental implantation and fetal growth.[16,65,66] AspH variants, such as R735Q/W, R688Q cause the ophthalmological condition-the Traboulsi syndrome[67–69] and the G434V variant causes vesicoureteral reflux (VUR).[70] The AspH gene is over-expressed in many cancer cells, in a manner proposed to promote cell migration and reduce the life expectancy of cancer patients; AspH is thus a promising target for anticancer therapy.[71–74] AspH is also hypoxically upregulated, and its kinetic parameters suggest it has potential as a hypoxia sensing enzyme, as known for some other 2OG oxygenases, including FIH.[75] Unveiling the catalytic strategy of AspH thus offers potential biotechnological applications, such as developing AspH-selective inhibitors that do not affect other Fe(II)/2OG enzymes and repurposing the enzyme for stereoselective C–H activation reactions. Such applications could be relevant, for example, for the efficient and sustainable synthesis of β-hydroxy acids/amides, which are structural motifs found in drugs, and biologically active molecules.[76]

In their resting state, most 2OG-dependent oxygenases contain a high-spin (HS) Fe(II) center in their active sites coordinated by a highly conserved structural motif, that is, the imidazole rings from two histidine-residues and one carboxylate from an aspartate- or glutamate-residue, sometimes called a 'facial triad'.[77–80] By contrast, AspH contains only two histidine Fe-ligands, and no carboxylate that coordinates the iron.[62,81] This arrangement is similar to the Fe(II)/2OG dependent halogenases, such as CytC3 (ref. 82) and SyrB2,[83,84] and the catalytically active D201G (but not D201A) variant of factor inhibiting HIF (FIH).[85] At the Fe(II) center of AspH, the normal carboxylate ligand is replaced by a coordinating water molecule (W1), the ligation of which is stabilized by a hydrogen bond with the SCS residue Asp721.[62] Multiple studies have evidenced the key role of the facial triad in catalysis by 2OG oxygenases;[86–88] however, how AspH catalysis proceeds with a dyad comprising only two histidine ligands, without the normal carboxylate ligand is unknown.

AspH is a multidomain protein (Fig. 1A) with a tetratricopeptide repeat (TPR) domain,[89] a hinge region, and an oxygenase (OXY) domain. The OXY domain contains a core



Fig. 1 Views from an AspH X-ray crystal structure (PDB ID: 5JZ8). (A) displays the OXY domain in blue, the TPR domain in pink, the hinge region in green, and the substrate in red. (B) QM/MM optimized structure with Fe(III) coordinated to the histidines (His679 & His725), 2OG, O₂, water (W1) (mode A). In mode A the Asp103$_{hFX}$ does not coordinate to the iron; instead, W1 coordinates the iron. (C) Mode B of the Fe(III)-superoxo complex, where the Asp103$_{hFX}$ coordinates the iron displacing a water molecule.

double-stranded beta-helix (DSBH) motif, which is flanked by several alpha-helices,[62] in a manner characteristic of 2OG oxygenases.[90,91] TPR domain has a functional role in substrate recognition. It is also present in other 2OG oxygenases such as collagen prolyl hydroxylases (CPH), some JmjC histone demethylases (KDM), *e.g.* ubiquitously transcribed X (UTX) and Y (UTY), and the leprecans.[92–95] The hinge region of AspH connects the OXY domain with the TPR domain.[62] Since substrate binding involves both the OXY and TPR domains, inter-domain dynamics and motions are expected to contribute to AspH catalysis.[96–100]

AspH hydroxylates EGFD substrates with a non-canonical disulfide pattern with disulfide links between Cys 1-2, 3-4, and 5-6, rather than the often observed canonical Cys 1-3, 2-4, 5-6 disulfide pattern.[62,64] The EGFD substrate of AspH considered in the present study was the N-terminal EGFD of human coagulation factor X (hFX), which has 39 amino acid residues (86–124), with a disulfide linkage between $Cys101_{hFX}$ and $Cys110_{hFX}$.[62] X-ray crystallographic studies have revealed two different aspartyl-residue substrate binding modes at the active site of the AspH enzyme-substrate (ES) complex. In the first binding mode (binding mode A, Fig. 1B), which most closely corresponds to the productive substrate binding in Fe(II)/2OG enzymes, $Asp103_{hFX}$ (the residue undergoing hydroxylation) of the EGFD hFX is not coordinated to the Fe(II). In the second binding mode B (Fig. 1C), which is likely an unproductive one, the $Asp103_{hFX}$ side chain carboxylate directly coordinates to the active site metal ion, trans to His725, displacing the coordinated water molecule.[62]

The mechanisms of 2OG oxygenases have been studied experimentally and computationally (Scheme 1).[80,101–123] The catalytic cycle is initiated by the co-substrate 2OG, then substrate binding to the Fe(II) center, followed by $O_2$ binding producing a Fe(III)-superoxo anion-radical (Fe(III)-OO•⁻) intermediate.[106,124] The latter reacts *via* a succinyl peroxide intermediate to give a ferryl (Fe(IV)=O) intermediate[125–130] with the formation of $CO_2$ and Fe-linked succinate. During hydroxylation, a substrate C–H hydrogen is abstracted by the Fe(IV)=O intermediate, *via* σ or π-channel electron transfer.[131] The resulting Fe(III)–OH intermediate undergoes rebound hydroxylation with the substrate radical, forming an alcohol and regenerating Fe(II). SCS and long-range (LR) interacting residues and correlated motions have been demonstrated to play important roles in the catalysis by non-heme Fe(II)/2OG enzymes controlling substrate binding and the catalytic mechanism.[57,58,132–139]

Although the mechanisms of 2OG oxygenases have been extensively studied, how AspH performs catalysis without the presence of the highly conserved facial triad has remained unknown. However, this is of great interest from the perspective of biocatalysis and for the development of selective inhibitors of AspH, as a cancer target.[71,73] Furthermore, the atomistic origins of the stereoselectivity of AspH for both aspartyl and asparaginyl- C–H hydroxylation are not understood. The role of the SCS and LR interacting residues in AspH catalysis, the complex dynamics of the EGFD substrate, and the interdomain motions of the AspH OXY and TPR domains are also unexplored, which could potentially guide in enzyme redesign.

To investigate the nature of catalysis by AspH, we performed molecular dynamics (MD) and quantum mechanics/molecular mechanics (QM/MM) studies. The results reveal how the protein dynamics, SCS, and LR interactions modulate the catalytic process in AspH and enable stereoselectivity without the canonical facial triad.

## Computational methods

### System preparation

A crystal structure of the human AspH ES complex with EGFD of hFX protein (PDB code: 5JZ8)[62] was used as the initial structure for the calculations. Missing residues of the substrate (Asp86-Gln98, Glu117-Phe124) were added using Modeller.[140,141]
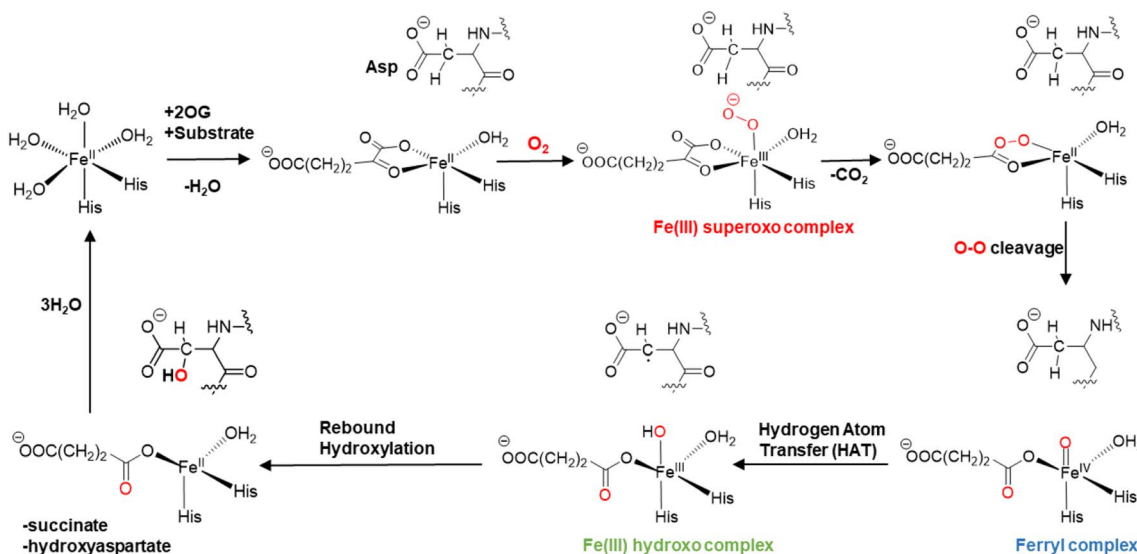


Scheme 1 Proposed catalytic cycle for AspH catalyzed hydroxylation.

Gaussview 6.0 was used to modify *N*-oxalglycine (NOG) (used for crystallization) to 2OG and to replace the active site Mn with Fe; Mn was used as an inert Fe substitute in the crystal studies. Propka[142] was used to determine the protonation states of the ionizable side chains, except for the Fe coordinating histidine residues and the Cys101$_{hFX}$, Cys110$_{hFX}$, Cys641, and Cys648 residues involved in disulfide bonds, were assigned after examining the local environment.

The active site parameters were prepared with Metal Center Parameter Builder (MCPB.py)[143] in Amber18.[144] Hydrogen atoms were added to the protein using the leap module in Amber, and Cl$^-$ counter ions were used to neutralize the system. Force constants for bonds and angles were obtained using the Seminario method,[145] while the point charge parameters for electrostatic potential were obtained using the RESP charge fitting (ChgModB) method.[146] Parameters for 2OG were generated using the Antechamber[147] module of Amber18. The system was then solvated using the Transferable Intermolecular Potential 3-Point (TIP3P)[148] water molecules in a box with a minimum of 10 Å between the protein surface and the box boundary. The geometry of nonheme iron systems was successfully reproduced in previous studies using the above-mentioned methods.[100,121,149] The parameters for the Fe(IV)=O complex were generated following a similar procedure, where monodentate succinate replaced the bidentate 2OG. The parameters for the D721A, R688A, K666A mutants were generated using the wild-type (WT) parameters by manual substitution of mutant residue.

## Molecular dynamics simulations

After solvating the system, a two-step minimization using MM was conducted. In the first minimization step, only solvent water molecules and Cl$^-$ counter ions were optimized; the solute (protein) was restrained using a 500 kcal mol$^{-1}$ Å$^{-2}$ harmonic potential. In the second step of the minimization, the restrain was removed from the solute, and all the atoms (solute + solvent) were optimized. Both minimizations were conducted for 5000 steps of steepest descent energy minimization followed by 5000 steps of conjugate gradient energy minimization.

After the two minimizations, the system was heated from 0 to 300 K for 50 picoseconds (ps) in a canonical (NVT) ensemble using a Langevin thermostat.[150] During heating, the solute molecules were restrained with a harmonic potential of 50 kcal mol$^{-1}$ Å$^{-2}$. After heating, the systems were kept at a constant 300 K in an isothermal-isobaric (NPT) ensemble for 1 ns with a restrain of 5 kcal mol$^{-1}$ Å$^{-2}$ placed on the solute molecules while the pressure of 1 bar was maintained. The productive MD calculations were conducted using the GPU version of Amber18 for a total of 1 μs at 1 bar with a pressure coupling of 2 ps. All the simulations were performed using the FF14SB[151] force field using periodic boundary conditions. A Berendsen barostat[152] was used to maintain the pressure, and the SHAKE algorithm[153] was used to constrain bonds involving hydrogen atoms. Long-range electrostatic interactions were calculated using the Particle Mesh Ewald (PME) method[154] with a direct space and vdW cut-off of 10 Å.

Root mean square deviation (RMSD), Root mean square fluctuations (RMSF), electrostatic interactions, and hydrogen bond analysis were done using the CPPTRAJ module from Ambertools utilities.[155] VMD[156] and Chimera[157] were used to analyze MD trajectories. Dynamic cross-correlation analysis (DCCA) and principal component analysis (PCA) were performed using Bio3D.[158]

## QM/MM calculations

All water molecules greater than 12 Å from the protein were stripped from the structures. The QM region for the Fe(III)-OO$^{\bullet-}$ intermediate includes Fe(III), O$_2$, 2OG, the imidazole groups of histidines His679 and His725, the coordinated water, and the substrate Asp103$_{hFX}$ (Fig. 2). For the Fe(IV)=O complex, O$_2$ was replaced with an oxo group and 2OG with succinate. The MM region was defined as all other protein atoms within 8 Å of the QM region and was described using Amber FF14SB forcefield. The positions of atoms beyond 8 Å from the QM region were fixed. We considered long-range electrostatic interactions for the QM/MM calculations using the electrostatic embedding scheme,[159] accounting for the polarizing effect of the MM region on the QM region *via* incorporation of the MM point charges in the Hamiltonian. The van der Waals interactions between MM and QM atoms are calculated using the Lennard-Jones potential. The QM/MM calculations were conducted using the Chemshell[160] package combining Turbomole[161] (QM region) and DL_POLY[162] (MM region). Hydrogen link atoms were used to cap the bonds spanning the boundary between the QM and MM regions using a charge shift model.[163–165] QM/MM geometry optimizations were performed using the Density Functional Theory (DFT) with the unrestricted B3LYP functional (UB3LYP) and def2-SVP basis set (termed B1) for all atoms defined in the QM part. A relaxed potential energy scan along the reaction coordinate in steps of 0.1 Å was performed from the optimized reactant complex (RC) to obtain transition states (TS) and intermediates using DL-find optimizer.[166] The highest energy points (TSs) were optimized without any constraints using the
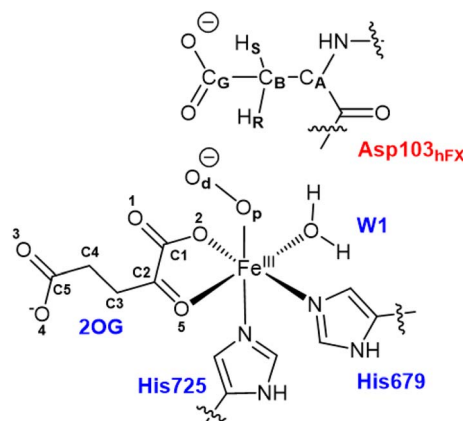


Fig. 2 QM region used for the QM/MM calculations of the AspH reaction mechanism includes Fe, 2OG (superoxo), O$_2$ (superoxo), succinate (ferryl), oxo (ferryl), side chain imidazole rings of Fe-ligating histidines (His679 and His725), W1 (mode A), Asp103$_{hFX}$.

dimer method[167] in Chemshell. Single-point energy calculations were also conducted with the larger basis set, def2-TZVP (B2) at the DFT UB3LYP level, to improve the calculated energy of each geometry. Frequency calculations were conducted for each optimized geometry to confirm all minima and TSs. Zero-point energy (ZPE) corrections obtained from frequency calculations were then added to the results of the single-point energy calculations to obtain energies reported as B3 (B2+ZPE). The empirical dispersion corrections were included in single-point energy calculations using Grimme's dispersion correction (D3)[168,169] with Becke-Johnson damping (D3-BJ).[170]

Spin Natural Orbital (SNO) analysis[171] was performed to analyze the molecular orbitals involved in the reaction path. TITAN code was used for electric field calculations.[172] Energy decomposition analysis (EDA)[173–175] was performed on optimized RCs and TSs to obtain total energy contributions/interaction energy ($\Delta E$) (van der Waals + electrostatic) of individual residues. The differences in the interaction energies between TS and RC structures ($\Delta\Delta E$) were calculated to investigate the contributions of individual residues on TS stabilization.

To evaluate the role of N-$C_A$-$C_B$-$C_G$ dihedral angle on stereoselectivity, an aspartate molecule with peptide linkages was optimized at the gas phase using DFT UB3LYP/def2SVP level, and the QM energy scan was performed at the same level of theory using N-$C_A$-$C_B$-$C_G$ dihedral as scan coordinate, using Gaussian 16 software.[176]

### QM/MM MD simulations

QM/MM MD simulation was performed with CP2K version 6.1, combining QUICKSTEPS (QM part) and FIST (MM part).[177,178] An equilibrated structure from the Fe(IV)=O classical MD simulation was used as the initial structure for QM/MM MD. The QM region used was the same as that used for the QM/MM calculations, and the remaining part of the system was treated as MM region. A real-space multigrid method was used to account for the electrostatic coupling between the QM and MM regions.[179,180] The DFT-D3 level of theory with B3LYP functional and the Gaussian and plane-waves method (GPW) with dual basis sets was used for the QM part.[178] The Gaussian double zeta valence polarized (DZVP) basis set[181] was used to describe the wave function, and the auxiliary plane-wave basis set expanded with a cut-off of 360 rydberg (Ry) and Goedecker–Teter–Hutter (GTH) potential was utilized to describe the electron density.[182] The auxiliary density matrix method (ADMM) was used to accelerate the Hartree–Fock exchange calculations.[183] The hydrogen link atom method was employed to complete the valences of the bonds at the QM-MM boundary.[163–165] The QM/MM MD simulation was performed in an NVT ensemble with a time step of 0.5 femtoseconds (fs) and for a total time of 5 ps.

## Results and discussion

### Structure and dynamics of the AspH Fe(III)-OO$^{\cdot-}$ ES complex for dioxygen activation

Conformational dynamics underlies the enzymes structure–function relationships by facilitating the substrate binding,

catalysis and product release.[184–194] To investigate the effect of the substrate binding mode on AspH catalysis, we performed MD simulations of the reactive AspH-Fe(III)-OO$^{\cdot-}$ complex in the two crystallographically observed substrate binding modes (modes A and B, Fig. 1B and C). RMSD, RMSF, and distance plots for both binding modes are provided in Fig. S1–S4 (ESI (ESI).† In both substrate binding modes A and B for the AspH-Fe(III)-OO$^{\cdot-}$ complex, the iron is coordinated by the co-substrate 2OG, two histidine residues (His725 and His679), $O_2$, and a water molecule (mode A) or the substrate (mode B). 2OG coordinates the iron in a bidentate fashion and is additionally stabilized by a network of interactions.[62] The network includes (i) a stable salt bridge between the 2OG C5 carboxylate and the Arg735 guanidium group and (ii) hydrogen bonding interactions of 2OG C1 carboxylate oxygens ($O_1$ and $O_2$) with the His690 imidazole –NH ($O_1$) and an Arg688 guanidium group –NH ($O_2$) as observed in the crystal structure, conserved in both binding modes A and B (Fig. S5†).

**The key role of SCS residue Asp721 in substrate binding mode A.** In binding mode A, the prochiral-(3R) hydrogen of Asp103$_{hFX}$ projects towards proximal oxygen ($O_p$) in the AspH-Fe(III)-OO$^{\cdot-}$complex; thus, this is more likely the productive conformation for catalysis. Asp721 plays a critical role in substrate positioning in AspH. The binding mode of W1, which replaces the facial triad carboxylate, is stabilized by hydrogen bonding with the Asp721 carboxylate side chain (Fig. S6 and S7†), as evidenced by crystallography (PDB: 5JZ8),[62] an arrangement that helps maintain a distorted octahedral geometry around iron. Asp721 also forms a stable salt bridge with the Arg686 guanidium group, and Arg686 also stabilizes substrate binding via electrostatic interaction with the Asp103$_{hFX}$ side chain carboxylate. The Asp721 backbone carbonyl also makes a stable hydrogen bonding interaction with the Gly681 main chain amide as present in the crystal structure and a solvent-mediated bridge hydrogen bonding with Thr683 observed from the MD, helps maintain the interactions of Asp721. Experimental studies show ∼80% reduction in the catalytic turnover of Asp721Ala (D721A) mutant compared to wild type (WT),[195] confirming the important but non-essential role of this residue in AspH catalysis.

**Conformational dynamics of AspH Fe(III)-OO$^{\cdot-}$ ES complex – substrate binding mode A.** In substrate binding mode A, the main chain amide groups of the two Fe(III)-coordinating histidine residues (His679, His725) form strong hydrogen bonds with each other, while their side chains interact with the main chain carbonyl of neighbouring protein residues; these interactions are maintained in all the studied complexes and likely enhance active site stability. His679 participates in a stable hydrogen bond with Trp677, and His725 in a stable hydrogen bond with Phe723. The Asp103$_{hFX}$ side chain carboxylate displays stable electrostatic interactions with the side chains of Arg688 and Lys666 (Fig. S9–S11†) and that of Arg686 (Fig. S9 and S12†), as observed in the crystal structure. A stable salt bridge between Arg688/Arg686 and the Asp741 side chain carboxylate is present throughout the simulation (Fig. S9†), which further stabilize the Asp103$_{hFX}$ orientation. The electrostatic interactions involving Asp103$_{hFX}$ help maintain a productive substrate

positioning for catalysis in the AspH active site. The non-canonical Cys 3-4 disulfide bridge (between Cys101$_{hFX}$–Cys110$_{hFX}$), which appears to play a critical role in substrate Asp103$_{hFX}$ positioning in the active site, is stabilized *via* hydrogen bonds with, the- Gly99$_{hFX}$ backbone carbonyl and the TPR residue, Tyr565 side chain hydroxyl groups (Fig. S13†).

The combined active site and substrate stabilizing interactions described here are consistent with those observed in the crystal structure; however, some interactions facilitating productive substrate orientation, as reported in the crystal structure, were weak throughout the AspH Fe(III)-OO$^{•−}$ MD. These include the Lys102$_{hFX}$–Asp616 salt bridge and the network of hydrogen-bonding interactions between residues-Gln627-Asp103$_{hFX}$, Glu617-Asp103$_{hFX}$, Glu615-Leu619, Arg686-Lys102$_{hFX}$ (See ESI for additional details†).

**Correlated motions in the AspH Fe(III)-OO$^{•−}$ complex – substrate binding mode A.** The DCCA for substrate binding mode A (Fig. 3A) shows that Asp721 exhibits a strong positive correlation with the motions of α12-α14, while anti-correlation with the movement of α2 of TPR, indicating a potential role of these regions in maintaining substrate binding. Importantly, the hinge region (~556–577), connecting the OXY and TPR domains, showed strong positive correlated motions with the Fe(III) coordinating residues (His679 and His725), SCS residue-Asp721, the substrate Asp103$_{hFX}$, and the substrate stabilizing residues Arg686, and Arg688, reflecting its importance in substrate binding. The role of the TPR domain in AspH substrate binding and catalysis exhibits similarities with that of the plant homeobox domain (PHD) in catalysis by the 2OG oxygenase KDM7B (PHF8).[196] The correlated motions of the PHD domain with the active site and SCS residues play a critical role in substrate binding and catalysis by PHF8,[57,100,122] suggesting that the TPR domain in AspH could perform a similar role. The substrate-stabilizing residues Arg686, Arg688, and the Cys101$_{hFX}$–Cys110$_{hFX}$ disulfide bridge showed strong anti-correlation with TPR α2-α4 helices. The intensive network of

correlated and anticorrelated motions suggests dynamic modulation of the enzyme–substrate interactions during catalysis. (See ESI for additional details†).

PCA (Fig. 3B) shows that the α2–α5 TPR helices move towards the substrate, possibly assisting in substrate positioning, while α7–α13, the hinge region, and α20 of the OXY domain move away from the substrate. The OXY domain shows movement towards the active site, potentially stabilizing the productive ES complex. The secondary structure of AspH, including the α helices and β sheets is provided in Fig. S14.†

Understanding the conformational dynamics of the ES complex provides vitally important information about key interactions in the SCS that might be catalytically important, as well as enlightens potentially intriguing LR interactions with RA residues that might be utilized for modulating, optimizing and repurposing the enzyme catalytic functions. The results align with earlier studies that demonstrated the role of dynamics for substrate binding, catalysis and as a valuable tool for enzyme engineering together with other computational and experimental approaches.[99,136,137,197–203]

**How the substrate Asp103$_{hFX}$ binding mode A influence the catalytic reaction of dioxygen activation?** The high spin quintet state of Fe(III)–O–O$^{•−}$ is reported to be the most favorable spin state for dioxygen activation in non-heme dioxygenases.[113,204–207] Hence, we performed QM/MM calculations only on the quintet spin state. Starting from mode A, the reaction followed the typical dioxygen activation mechanism for 2OG oxygenases (Scheme S1†). 2OG decarboxylation, *via* C1–C2 2OG bond cleavage following nucleophilic attack of the distal oxygen (O$_d$) of the Fe(III)–O–O$^{•−}$ on the 2OG carbonyl C2, forms the peroxosuccinate intermediate (IM1). The process requires 8.9 kcal mol$^{-1}$ activation energy, and IM1 is stabilized by −38.8 kcal mol$^{-1}$ (Fig. S15†). In the second step, the Fe(IV)=O intermediate is formed *via* peroxosuccinic O–O cleavage which requires 2.0 kcal mol$^{-1}$ activation energy, and the Fe(IV)=O is stabilized by −46.6 kcal mol$^{-1}$ (Fig. S15†). Thus, the
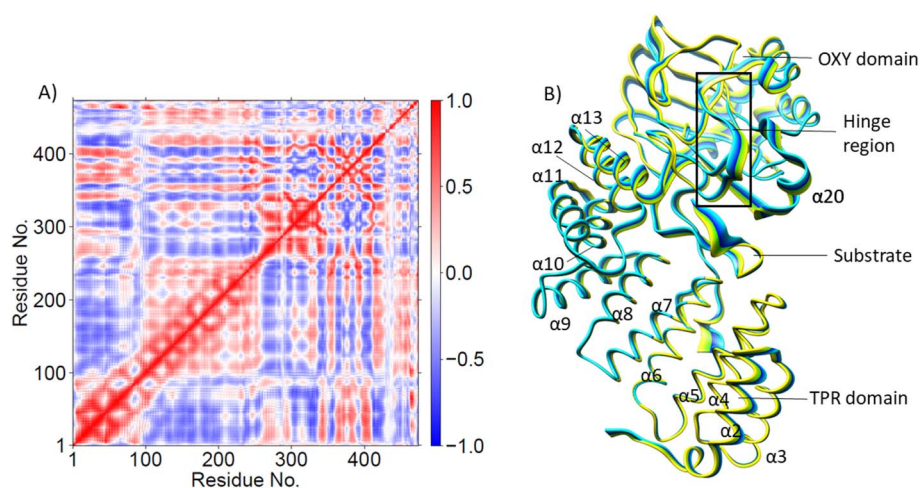


**Fig. 3** (A) Dynamic Cross Correlation Analysis (DCCA) and (B) Principal Component Analysis (PCA) of C$_α$ atoms in the AspH Fe(III)-OO$^{•−}$ complex (binding mode A). Residues 1-429 are AspH protein residues; 430-Fe, 431-O$_2$, 432-2OG, 433-W1. Residues 434–472 are EGFD substrate residues; 451-Asp103$_{hFX}$. The motion of the residues in PCA (part B) is indicated by the color change from yellow to blue.

decarboxylation step is the rate-limiting during the dioxygen activation process, in accord with the previous studies on 2OG oxygenases.[80,121,122,208–211] Fig. S16† displays the geometric parameters and spin densities of stationary points involved in dioxygen activation *via* binding mode A (See ESI for additional details†).

**How the substrate binding mode B influence the dioxygen activation?** In binding mode B of the superoxo ES complex (Fig. 1C), the substrate Asp103$_{hFX}$ binds to Fe(III) trans to His725, and O$_2$ can potentially bind to the vacant coordination site trans to the C2 carbonyl group of 2OG. MD simulations reveal that most of the active site and SCS interactions are similar for both ES complexes of binding modes A and B. Key differences include weaker electrostatic interactions involving Asp103$_{hFX}$ side chain carboxylate and Lys666 and Arg686 in mode B (Fig. S11 and S12†). Notably, the average superoxide O$_d$–C2 distance, critical for the dioxygen activation is 5.91 Å in binding mode B compared to 3.67 Å in binding mode A (Fig. S4†).

QM/MM calculations for the reaction of dioxygen activation starting from binding mode B give a very high barrier of 75.2 kcal mol$^{-1}$ for the superoxide nucleophilic attack on C2 and the formed peroxosuccinate intermediate is exothermic to RC1′ (Fig. S17†). The reason for such high energy is that the Asp103$_{hFX}$ coordination to the Fe(III) center keeps the O$_2^{•-}$ trans to the C2 of 2OG, thus requiring a significant structural rearrangement for the nucleophilic attack by superoxide onto C2 of 2OG, rendering oxidative decarboxylation highly unfavourable for binding mode B. The geometric parameters for dioxygen activation in binding mode B are given in Fig. S18.†

In summary, reaction path calculations starting from binding modes A and B confirm that the substrate Asp103$_{hFX}$ carboxylate should not be coordinated to the Fe(III) center for productive dioxygen activation reaction in agreement with proposed mechanisms for most 2OG oxygenases.[100,106,108,121,123,127,138,208,212,213]

## Structure and dynamics of the ES complex for the stereospecific Asp hydroxylation

Dioxygen activation *via* substrate binding mode A leads to the formation of the AspH Fe(IV)=O-EGFD complex (RC2 (Scheme 2)/IM3 (Scheme S1†)), which is the intermediate necessary for Asp103$_{hFX}$ hydroxylation. Fig. S19–S22† display the RMSD, RMSF, key distances, and angle plots for Fe(IV)=O intermediate. MD simulations revealed that most active site interactions remained similar in the Fe(III)-OO$^{•-}$ and Fe(IV)=O intermediates (Fig. S7–S12†). Key differences include the stable hydrogen bonding of Arg688 guanidium NH with W1 and the Ser668 side chain hydroxyl with Fe(IV)-linked succinate C4 carboxylate in the Fe(IV)=O complex, which were less prominent in the Fe(III)-OO$^{•-}$ complex (Fig. S23†). Further, the Arg735:2OG C5 carboxylate salt bridge observed in Fe(III)-OO$^{•-}$ complex is disrupted upon succinate formation in Fe(IV)=O complex, possibly due to a shorter carbon length in succinate. Instead, a stable solvent-mediated bridging hydrogen bond is observed between Arg735 side chain guanidium NH and the C4

carboxylate of succinate in the Fe(IV)=O complex. A stable solvent-mediated (W2) bridging hydrogen bond between the ferryl O$_p$ and Asp721 side chain carboxylate helps orientate the Fe(IV)=O oxygen towards the pro-R hydrogen of Asp103$_{hFX}$ C$_B$ (Fig. S24†). Overall, most active site interactions, particularly those involved in substrate positioning in the Fe(III)-OO$^{•-}$ simulation, also appear stable in the Fe(IV)=O simulation, indicating tight substrate binding.

DCCA analysis revealed that most correlated motions in the AspH Fe(IV)=O and Fe(III)-OO$^{•-}$ complexes are similar (Fig. 4A). In the AspH Fe(IV)=O complex, Asp721 showed a positive correlation with that of α19 of the OXY domain and the loop residues connecting α19 with βI of DSBH, and anti-correlation with the motions of helices α4 and α6 of the TPR domain. The 2OG/succinate stabilizing residues Arg735 and Ser668 display a strong positive correlation with TPR helices α1-α4. Substrate stabilizing residue Arg688 and 2OG stabilizing residue Arg735 exhibited strong anti-correlation with the motions of TPR helices α6 and α7 in the Fe(IV)=O complex, not observed in the Fe(III)-O-O$^{•-}$ complex. Thus, the LR interactions of helices α6 and α7 with the 2OG, and substrate stabilizing residues likely play a crucial role in AspH catalysis. Interestingly, kidney dysfunction in humans is caused by a mutation of AspH Gly434 residue, which forms the loop connecting α6 and α7. These observations highlight the roles of the TPR domain not only in substrate binding, but also in dynamic motions during catalysis, potentially in a similar manner as with other 2OG oxygenases such as collagen prolyl hydroxylases.[92]

PCA analysis also reveals that the AspH Fe(IV)=O complex is less flexible than the Fe(III)-OO$^{•-}$ complex (Fig. 4B), arising from the stronger substrate and active site stabilizing interactions observed in the Fe(IV)=O simulation. The TPR domain displayed movement towards the substrate and the OXY domain, potentially contributing to the compactness of the Fe(IV)=O complex. The limited flexibility and motions of helices α2-α13 and the hinge region may contribute to a more rigid OXY domain and tight binding of the substrate, as evidenced by their correlated movements with substrate stabilizing residues. Overall, the PCA depicts a more rigid and contract Fe(IV)=O complex than the Fe(III)-OO$^{•-}$ in a manner likely favoring catalysis.

To examine the dynamic behavior of the Fe-coordinated water molecule during the catalytic reaction, we performed a QM/MM MD simulation of the Fe(IV)=O intermediate. This type of simulation combines exploration of dynamics/flexibility and changes in electronic structure (such as bond breaking and creation). The simulation shows that the distance between the Fe and the coordinated water molecule remains very stable (an average Fe–W1 distance of 2.12 Å, Fig. S25A†). This indicates that W1 remains firmly coordinated to Fe and does not diffuse away. To further elaborate on the strength of the coordination of W1, we performed a QM/MM potential energy surface (PES) study of the dissociation of W1 from the iron center (Fig. S25B†). The PES scan indicates that the dissociation of W1 is very unfavored leading to a continuous increase of the energy, further indicating that there is no spontaneous water

Scheme 2  Proposed mechanism of AspH catalyzed substrate hydroxylation.

dissociation and formation of a four-coordinate (4C) ferryl complex and that such a process would require high activation energy. We also evaluated if a second solvent water molecule could displace W1 from Fe (Fig. S25C†); however, the high barrier observed for this process suggests such a ligand exchange may not be feasible in the Fe(IV)=O intermediate state (Fig. S25C†). Therefore, the coordination of W1 to Fe is essential to form the catalytically productive Fe(IV)=O intermediate and to enable the C–H activation.

### Mechanism of the stereospecific Asp hydroxylation

AspH substrate hydroxylation from the Fe(IV)=O complex proceeds in two steps: (1) hydrogen atom transfer (HAT) from the β-carbon ($C_B$) of $Asp103_{hFX}$ by the Fe(IV)=O group, and subsequent (2) rebound hydroxylation producing 3-hydroxy-L-aspartate (Scheme 2). The energy profile for HAT and rebound hydroxylation steps is given in Fig. 5. We optimized the Fe(IV)=O intermediate in triplet and septet states using the same level of theory used for the quintet calculations (Fig. 5). The results show that the quintet state of the Fe(IV)=O intermediate is energetically more favorable compared to triplet and septet states, agreeing with prior studies on Fe(II)/2OG

oxygenases.[80,122,129,207,214,215] During HAT, a single electron transfers from the substrate pro-R C–H bond to the Fe(IV)=O moiety, resulting in $C_B$–$H_R$ bond cleavage and alkyl radical (IM4) formation. At the same time, Fe(IV) is reduced to Fe(III)–OH. The activation barrier for pro-R HAT is 20.8 kcal mol$^{-1}$ (at B3 level). The electron transfer can occur either through a π or σ channel.[131,204,215] The σ channel involves a transfer of an α electron (electron with a magnetic spin quantum number ($m_s$) of $+\frac{1}{2}$) from the substrate $\sigma_{C-H}$ orbital to the Fe $\sigma^{*}z^2$ orbital, leaving a β electron (electron with a $m_s = -\frac{1}{2}$) on the substrate radical. The head-on overlap of the two σ orbitals results in a more linear Fe–O–H arrangement with an approximate bond angle larger than 120° and closer to 180°.[204] Conversely, in the π channel, a β electron from the substrate transfers into the antibonding metal $\pi^{*}_{xz/yz}$ orbital through angular overlap resulting in a Fe–O–H bond angle approaching 120°.[204] SNO analysis (Fig. 6) of the HAT TSs shows that C–H α electron from the substrate transfers to the Fe(IV)=O $\sigma^{*}_{z^2}$ orbital, and a β electron remain at the carbon radical, suggesting a σ channel mechanism (Fig. 7) in AspH. In $TS_{proR}$, the Fe–O bond elongates to 1.77 Å (from 1.64 Å in RC2), and the $C_B$–$H_R$ bond
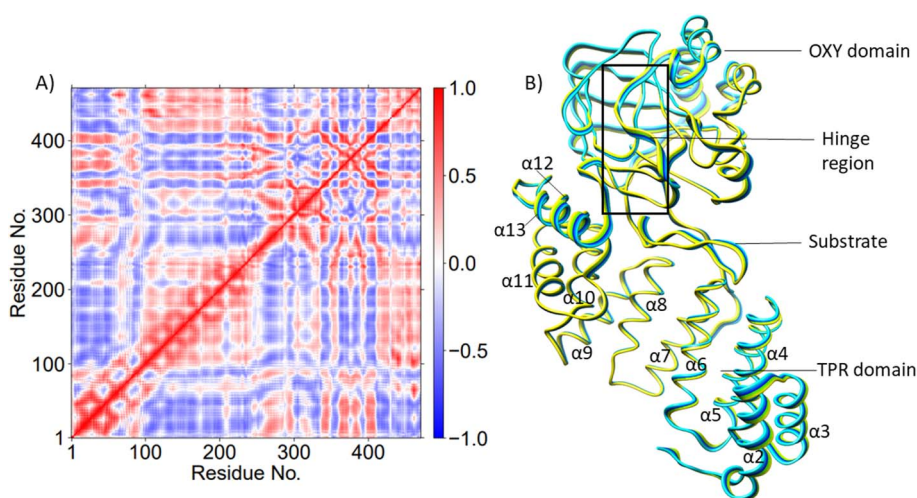


Fig. 4  (A) Dynamic Cross Correlation Analysis (DCCA) and (B) Principal Component Analysis (PCA) of $C_\alpha$ atoms in the AspH Fe(IV)=O complex. Residues 1-429 are AspH protein residues; 430-Fe, 431-$O_p$, 432-succinate, 433-W1. Residues 434-472 are EGFD substrate residues; 451-$Asp103_{hFX}$. The motion of the residues in PCA (part B) is indicated by the color change from yellow to blue.

Fig. 5 Energy profile for the pro-R (blue) and pro-S (red) HAT and rebound hydroxylation steps calculated at UB3LYP/def2-TZVP (B2) (red) and B2 +ZPE (B3) (black).



Fig. 7 Electron transfer and orbital occupancy during the HAT step.

elongates to 1.34 Å (from 1.11 Å in RC2), while the $O_p$–$H_R$ distance shortens to 1.32 Å from 3.18 Å (RC2) (Fig. 8). In IM4, Fe is antiferromagnetically coupled to the substrate radical, as indicated by the spin densities of 4.22 (Fe), 0.27 ($O_p$), and −0.35 ($C_B$) (Fig. 8).

### How do SCS residues sterically stabilize the HAT TS

Electrostatic interactions of SCS residues, Lys666, Arg686, and Arg688, help stabilize the side chain carboxylate of $Asp103_{hFX}$ in the HAT TS (Fig. 9). Additionally, hydrogen bonding between the $Asp103_{hFX}$ side chain carboxylate and the Gln664 side chain NH; the solvent-mediated bridging hydrogen bonding interactions of residues Asp721 and W1; the bridging hydrogen bonding interaction of water molecule (W2) with Asp721, the oxo moiety, and the $Gly104_{hFX}$ backbone NH group of the

substrate, are likely involved in productive substrate positioning and TS stability (Fig. 9). Solvent-mediated hydrogen bond interactions with the Fe(ɪv)═O moiety have been observed in other 2OG oxygenases, such as AlkB[216] and TET2.[138] This interaction may contribute to the observed stereoselectivity in AspH by aligning the Fe═O moiety towards the pro-R hydrogen of $Asp103_{hFX}$.

### How the flexibility of the RC influences the HAT reaction?

To explore how the conformational flexibility of the RC influences the HAT step, we performed QM/MM calculations using five different MD snapshots of the Fe(ɪv)═O intermediate. Tables S1 and S2† show geometric parameters and spin densities variation for the different HAT TSs. The Fe–$O_p$, $C_B$–$H_R$ and O–$H_R$ bond distances range from 1.76–1.79 Å, 1.34–1.47 Å, and 1.24–1.32 Å respectively, while the Fe–O–$H_R$ angle varies from 156.59°–171.91° in different HAT TSs. The calculated Fe–$O_p$–$H_R$ angle values, the $Asp103_{hFX}$ $C_B$ spin densities in the different pro-R HAT TS structures (−0.37 to −0.29), and SNO analysis indicate that the σ-channel mechanism is exclusively used by AspH. The bond angles and spin densities for HAT TSs



Fig. 6 Spin Natural Orbitals (SNO) with corresponding electron occupancies (in brackets) for the HAT TSs: (A) $TS_{proR}$ and (B) $TS_{proS}$.
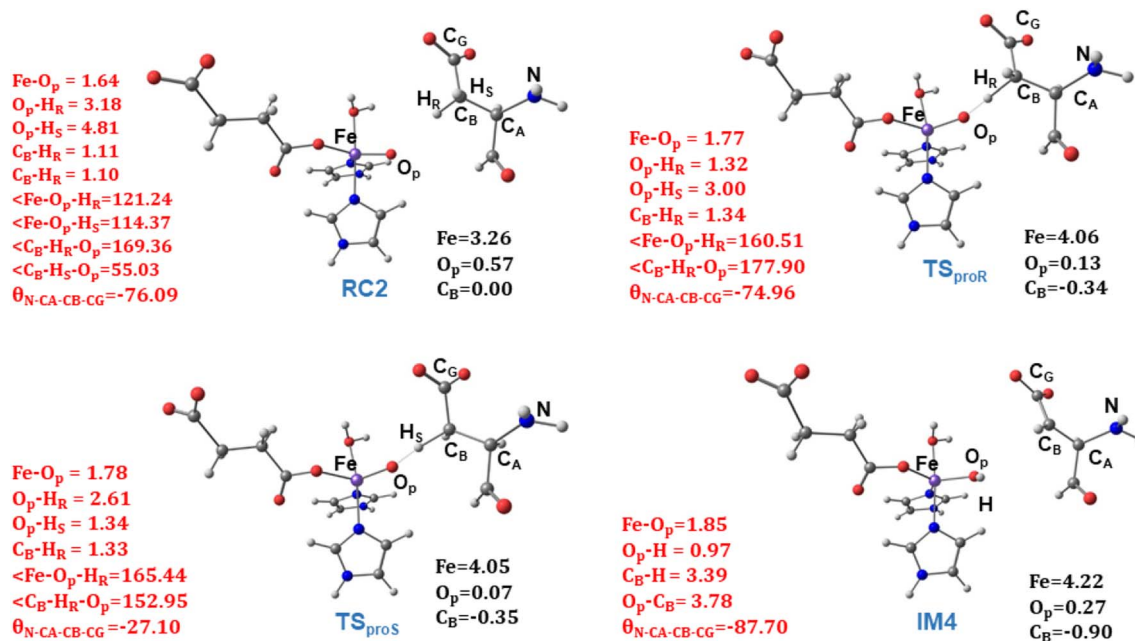
**Fig. 8** Geometric parameters (red) and spin densities (black) of optimized stationary points in HAT step.

corroborate with that of studied 2OG oxygenases such as AlkB/AlkBH2,[113,121] TET2,[138,200,217] TauD,[139,218,219] KDM4A,[123] KDM6B,[220] KDM7B (PHF8)[122] that follow $\sigma$-channel mechanism. The calculated electronic energy barriers for the HAT step varied from 20.8 to 25.8 kcal mol$^{-1}$ (Table 1 and Fig. S26†) with a Boltzmann weighted average of 21.5 kcal mol$^{-1}$ (B3 level). The computed barriers with dispersion corrections (D3-BJ) for representative snapshots (snapshot1 and snapshot 4) show barriers 19.4 kcal mol$^{-1}$ and 23.4 kcal mol$^{-1}$, respectively at the B3 level (Table S3†). The HAT barriers observed in experimental and computational studies on other Fe(II)/2OG oxygenases like prolyl-4-hydroxylase (20.7 kcal mol$^{-1}$),[114,221] TauD

(23.2 kcal mol$^{-1}$),[222] histone demethylases (20.2–25.2 kcal mol$^{-1}$),[122,123,220,223] and DNA-demethylases (15.5–26.7 kcal mol$^{-1}$),[121,138,214,224,225] align with the barriers we have calculated for AspH.

Notably, the HAT barriers and reaction energies show a positive correlation with the strength of the hydrogen bonding between W2 and the O$_P$ and a negative correlation between that of W1 and Asp721 (Table S4 and Fig. S27–S30†). In the snapshots where W2–O$_P$ hydrogen bond is stronger, a higher stability for IM4 and a lower HAT barrier are observed. Therefore, the presence of the carboxylate residue-Asp721 in the SCS is vital in HAT TS stabilization and modulating the HAT rate. All
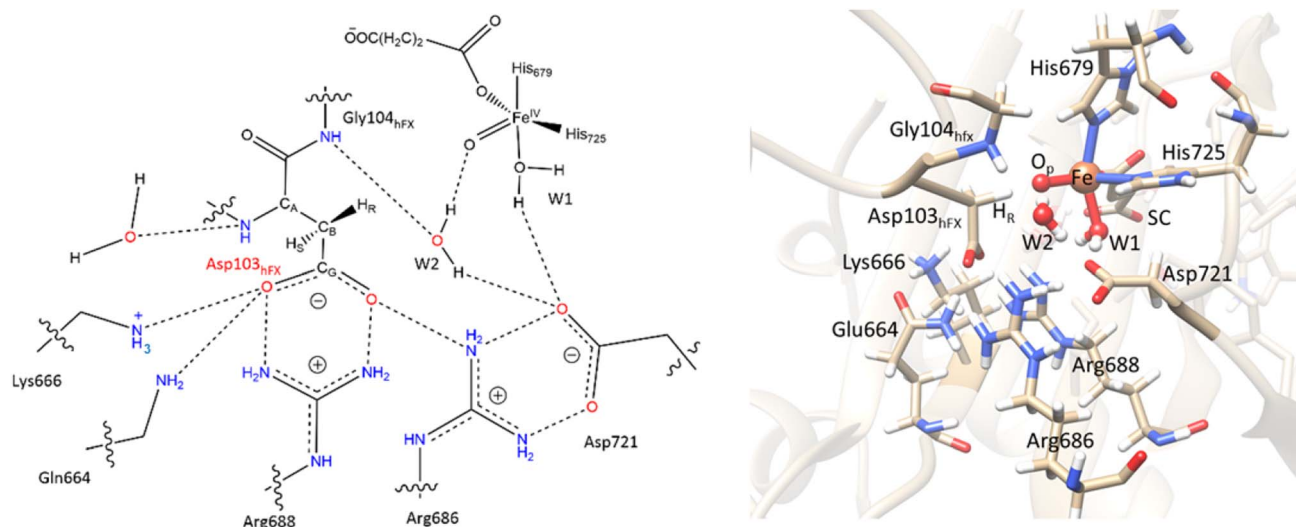


**Fig. 9** SCS interactions restricting the rotation of Asp103$_{hFX}$ N-C$_A$-C$_B$-C$_G$ dihedral and positioning pro-R H atom towards the Fe(IV)=O moiety.

**Table 1** Activation barriers and reaction energies for the HAT step

| AspH-WT | | Activation barrier | | | Reaction energy | | |
|---|---|---|---|---|---|---|---|
| | | B1 (kcal mol$^{-1}$) | B2 (kcal mol$^{-1}$) | B3 (kcal mol$^{-1}$) | B1 (kcal mol$^{-1}$) | B2 (kcal mol$^{-1}$) | B3 (kcal mol$^{-1}$) |
| Snapshot 1 | HAT$_{proR}$ | 22.0 | 24.9 | 20.8 | −9.3 | −11.3 | −9.7 |
| | HAT$_{proS}$ | 42.3 | 45.1 | 42.1 | −9.3 | −11.4 | −9.9 |
| Snapshot 2 | HAT$_{proR}$ | 22.2 | 25.7 | 21.1 | −10.0 | −11.6 | −9.8 |
| | HAT$_{proS}$ | 41.1 | 46.1 | 42.4 | −9.9 | −11.5 | −9.9 |
| Snapshot 3 | HAT$_{proR}$ | 24.4 | 26.9 | 25.8 | −5.8 | −7.6 | −2.9 |
| | HAT$_{proS}$ | 42.8 | 46.3 | 44.6 | −5.5 | −7.9 | −7.1 |
| Snapshot 4 | HAT$_{proR}$ | 26.7 | 30.2 | 25.4 | −2.7 | −4.5 | −3.9 |
| | HAT$_{proS}$ | 45.2 | 49.0 | 44.9 | −2.7 | −4.6 | −3.8 |
| Snapshot 5 | HAT$_{proR}$ | 26.2 | 28.8 | 25.3 | −4.0 | −7.2 | −2.2 |
| | HAT$_{proS}$ | 41.3 | 44.8 | 42.2 | −4.0 | −7.2 | −2.2 |

the five snapshots revealed HAT to be exothermic with reaction energies in the range −9.8 to −2.2 kcal mol$^{-1}$ at B3 level. The Fe(III)–OH hydroxyl moiety in IM4 is stabilized by hydrogen bonding with W2. The EDA (Fig. S31†) manifests that IM4 is stabilized by the SCS residues Arg688, Lys666, and Asp721 (Fig. S32†), by energy contributions of −1.5, −1.3, and −4.7 kcal mol$^{-1}$, respectively.

### Protein control on the stereoselectivity in the HAT

To investigate the origin of stereoselectivity, we performed QM/MM reaction path calculations for the pro-S HAT using the same starting snapshots used for the Fe(IV)=O intermediate RC2 as for the pro-R HAT reaction (Fig. 5). Unlike the pro-R HAT, we found that the pro-S HAT is unfeasible due to a relatively high activation barrier of 42.1 kcal mol$^{-1}$. We observed that the activation barrier for pro-S HAT is consistently high across all five snapshots, with energy differences between pro-R and pro-S HATs ranging from 15.1–20.3 kcal mol$^{-1}$ at the B1 level and 16.9–21.3 kcal mol$^{-1}$ at the B3 level (Table 1). A superimposed structure of TS$_{proR}$ and TS$_{proS}$ is given in (Fig. S33†). The dihedral angle (N-C$_A$-C$_B$-C$_G$) is a key structural determinant between the TS$_{proR}$ and TS$_{proS}$ geometries, with the former having a dihedral angle of −74.96° and the latter having a dihedral angle of −27.10°, compared to −76.09 in RC2 for snapshot 1. N-C$_A$-C$_B$-C$_G$ dihedral angle varies from −83.33 to −71.40° in TS$_{proR}$, −29.71° to −16.55° in TS$_{proS}$, and −76.77° to −72.89° in RC2 (Table S2†). We further performed a QM energy scan to investigate the role of this dihedral angle and the stability of the geometry of the substrate Asp-residue (Fig. S34†). The scan revealed that a change of the N-C$_A$-C$_B$-C$_G$ dihedral from a pro-R TS value of −74.96° to a pro-S TS value of −27.10° requires a barrier of ~9 kcal mol$^{-1}$, calculated at the UB3LYP-def2SVP level, corresponding to a QM/MM energy difference of 15.1–20.3 kcal mol$^{-1}$ (at B1 level), suggests that the increased stability (between 6.1 and 11.3 kcal mol$^{-1}$) of the pro-R compared to the pro-S orientation arises from the interactions with the AspH protein environment that restraints the substrate to favor pro-R HAT. The Asp103$_{hFX}$ side chain carboxylate interacts with Arg686, Arg688, and Lys666 *via* electrostatic

interactions and Gln664 side chain amine *via* hydrogen bond. In addition, the Gly104$_{hFX}$-Asp721 solvent-mediated hydrogen bond and the hydrogen bonding interaction of the Asp103$_{hFX}$ backbone amide with solvent water promotes pro-R HAT (Fig. 9). The substantial geometric changes required to reach TS$_{proS}$ from RC2 result in a high activation barrier, thereby disfavoring pro-S HAT. Interestingly, the pro-R and pro-S HAT reactions lead to the same intermediate (IM4), with an N-C$_A$-C$_B$-C$_G$ dihedral angle of −87.70°, still preferring the pro-R product. The pro-S configuration of IM4 is also destabilized by repulsive interactions between hydrogen atoms on Asp103$_{hFX}$ C$_B$ and C$_A$ atoms. Thus, the overall stereoselectivity of the AspH hydroxylation reaction is determined by the HAT step.

Substrate positioning is a critical factor in determining stereoselectivity.[139] We further performed EDA on both pro-R and pro-S HAT TSs to investigate the role of SCS residues in determining stereoselectivity. We calculated the differential contributions between each TS (pro-R and pro-S) and the RC2 and then calculated the difference between the two differential contributions ($\Delta E$ (TS$_{proR}$ − RC2) − $\Delta E$ (TS$_{proS}$ − RC2)). A positive $\Delta$ ($\Delta\Delta E$) value indicates destabilizing, while a negative value indicates stabilizing effect on the TS$_{proR}$ (Fig. S35†). We found that the SCS residues Gln664, Arg686 and Arg688 influence stereoselectivity by showing stronger energetic contributions towards stabilizing the pro-R TS compared to the pro-S TS *via* hydrogen bonding (Gln664) and electrostatic (Arg686 and Arg688) interactions (Fig. S36†). Comparing TS$_{proR}$ and TS$_{proS}$ structures, we observed that the positioning of the Arg688/Arg686/Lys666 sidechain-Asp103$_{hFX}$ carboxylate salt bridges and Gln664 hydrogen bond influences the Asp103$_{hFX}$ carboxylate position and the orientation of the pro-R hydrogen with respect to the Fe(IV)=O moiety to enable stereoselective reaction (Fig. 9). The revealed significant differential catalytic contributions by SCS residues towards stabilizing the pro-R and pro-S TS offer opportunities for engineering novel enzymes or catalysts for stereoselective C–H activation reactions. Furthermore, DCCA analysis of the ferryl complex suggests that the motions of TPR domain helices α2-α7 and α12-α14, as well as OXY domain helices α16, α18, and α19 all involved in substrate binding, show correlations with SCS residues involved in TS$_{proR}$

and $TS_{proS}$ stabilization, indicating that these residues could also influence the stereochemical outcome of the reaction *via* LR interactions (Fig. S37–S40†), thus providing an intriguing new background for long-range allosteric modulation of AspH activity and stereoselectivity.

Reaction selectivity in enzymatic catalysis can be influenced by electrostatic preorganization, that is the orientation of enzyme's internal electric fields (IEFs).[226,227] To evaluate the effect of IEF on stereoselectivity in AspH, the net electric field along the Fe=O axis was calculated for both pro-R and pro-S HAT (Table S5†). In all five snapshots, the net IEF along the Fe=O axis was more negative for $TS_{proS}$ than the corresponding $TS_{proR}$, indicating the role of EF in stereoselectivity and modulating the EF along the Fe=O direction could be a strategy to alter the stereoselectivity in AspH.

## Rebound hydroxylation

At the final stage of the reaction mechanism, substrate hydroxylation proceeds through a radical rebound mechanism, where the hydroxyl group from the Fe(III)–OH intermediate (IM4) transfers to the substrate methylene radical generated after HAT. Subsequently, Fe(III) reduces to Fe(II), and the hydroxylated product forms. Rebound hydroxylation shows a 27.8 kcal mol$^{-1}$ barrier relative to the stable intermediate IM4 (RC3 in Fig. S41†), corresponding to the lowest energy HAT pathway (snapshot 1) at the B3 level. All five QM/MM snapshots revealed a similar high activation barrier for the rebound step (Table 2 and Fig. S41†) with a Boltzmann weighted average of 26.4 kcal mol$^{-1}$ at the B3 level of theory, suggesting this step may be rate-limiting in AspH instead of the HAT step which is the most common rate-limiting step in Fe(II)/2OG enzymes.[113,114,121,122,138,175,228] Calculations with dispersion corrections (D3-BJ) show a decrease in the B3-level rebound barriers to 25.5 and 23.4 kcal mol$^{-1}$ for representative snapshots (snapshot 1 and snapshot 4), respectively (Table S6†). Both the HAT and rebound reactions require changes in the torsional angle N-$C_A$-$C_B$-$C_G$ of the substrate Asp103$_{hFX}$ (from the respective RCs to the TSs). However, this change is much larger for the rebound step and respectively requires larger energy. In the HAT, during the transition from RC2 to $TS_{proR}$ (snapshot 1), the torsional angle changes from −76.09 to −74.96 degrees (Table S2†). In contrast, for the rebound step, the torsion angle changes from −87.70 (in the IM4) to −79.55 degrees (in the $TS_{REB}$) (Table S8†). A similar trend is observed across five different snapshots (see Tables S2 and S8†). Such a significant

torsional adjustment disturbs the salt bridge and hydrogen bonding interactions that tightly bind the Asp103$_{hFX}$ side chain carboxylate and contribute to the higher energy barrier observed for the rebound step compared to the HAT. Previous studies by Shaik *et al.* describe a case of rebound hydroxylation as rate limiting in CYP450 catalyzed reaction of dopamine formation.[229] Similarly, Lu *et al.* reported a higher barrier for rebound step than for HAT in the TET2-catalyzed conversion of 5-methylcytosine to 5-hydroxymethylcytosine.[224] Furthermore, in nonheme Fe(II)/2OG halogenases, which lack the facial triad carboxylate, a relatively high barrier was observed for the rebound hydroxylation compared to halogen atom transfer which is important in distinguishing reaction selectivity between hydroxylation and halogenation.[202,230–232] The finding that the rebound reaction was predicted to be the rate-limiting step in other heme/non-heme enzymes with conventional coordination suggests that other factors than the water coordination might be responsible for the high energy barrier of the rebound hydroxylation, however further studies would be necessary to comprehensively explore this issue.

$TS_{REB}$ represents the TS for rebound hydroxylation (Fig. 10), wherein the Fe–$O_P$ distance elongates to 2.20 Å, and the $O_P$–$C_B$ distance reduces to 2.23 Å from 1.85 Å and 3.78 Å respectively, in IM4. The N-$C_A$-$C_B$-$C_G$ dihedral decreases to −79.55 ($TS_{REB}$) from −87.70 (IM4), and the hydroxyl $O_P$ to $C_B$ (Asp103$_{hFX}$) distance decreases to 2.27 Å from 3.78 Å. Tables S7 and S8† show the spin densities and geometric parameters of all stationary points involved in the rebound step. The hydroxyl moiety in $TS_{REB}$ is stabilized by the solvent-mediated (W2) bridging hydrogen bond with Asp721. As the hydroxyl radical leaves the Fe center, W2 coordinates to the vacant position to generate a stable Fe(II) complex. The hydroxylation product is exothermic by −31.4 kcal mol$^{-1}$ (Fig. 5), which compares favorably well with previous studies on other non-heme Fe(II)/2OG oxygenases.[114,120–123,138,219,230,233]

EDA shows $TS_{REB}$ is stabilized by residues Asp721 (−1.4 kcal mol$^{-1}$), Lys666 (−0.9 kcal mol$^{-1}$), and Asp741 (−1.9 kcal mol$^{-1}$), and destabilized by Arg688 (3.5 kcal mol$^{-1}$) and Arg686 (0.8 kcal mol$^{-1}$) (Fig. S42–S44†) compared to IM4.

## Effect of the D721A mutation on substrate binding and hydroxylation

To explore the importance of Asp721, we performed MD with D721A, which manifests substantially reduced catalytic activity.[195] MD for D721A shows an overall increase in the

**Table 2** Activation barriers and reaction energies for the rebound hydroxylation step

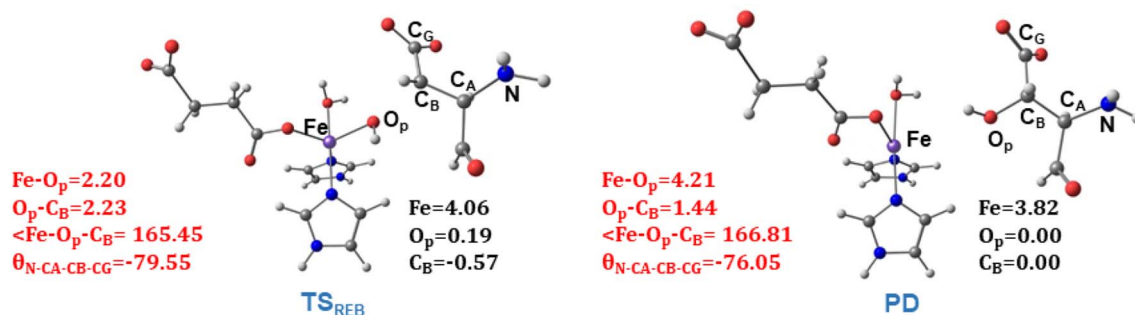| AspH-WT | Activation barrier | | | Reaction energy | | |
|---|---|---|---|---|---|---|
| | B1 (kcal mol$^{-1}$) | B2 (kcal mol$^{-1}$) | B3 (kcal mol$^{-1}$) | B1 (kcal mol$^{-1}$) | B2 (kcal mol$^{-1}$) | B3 (kcal mol$^{-1}$) |
| Snapshot 1 | 26.6 | 30.8 | 27.8 | −41.2 | −40.0 | −31.4 |
| Snapshot 2 | 28.2 | 33.3 | 30.7 | −35.3 | −32.4 | −24.1 |
| Snapshot 3 | 24.8 | 30.2 | 26.9 | −40.5 | −36.1 | −24.7 |
| Snapshot 4 | 22.2 | 28.7 | 25.8 | −35.3 | −30.4 | −22.3 |
| Snapshot 5 | 26.3 | 32.5 | 28.1 | −34.7 | −32.2 | −21.6 |

**Fig. 10** Geometric parameters (red) and spin densities (black) of optimized stationary points in rebound hydroxylation step.

average distance between $Fe(IV)=O$ $O_p$ and the substrate $C_B$ of 7.03 Å compared to 4.23 Å to the AspH-WT. The increased distance between the $Fe(IV)=O$ oxygen and the substrate leads to enhanced flexibility of the ES complex (Fig. S45–S47 and Table S9†), disrupting the ES complex stabilizing salt bridges. PCA shows that $Fe(IV)=O$ complex for D721A has motions opposite to that of the WT (Fig. S48A†). Specifically, the hinge region and the TPR domain helices show movement away from the active site, making the OXY domain in the D721A mutant less compact. The α1–α5 and α10–α13 helices in the TPR domain move away from the substrate in the D721A mutant, consequently increasing the distance between $O_p$ and $C_B$. Therefore, Asp721 acts as an SCS alternative for the missing facial triad carboxylate in AspH, stabilizing the active site and for productive substrate binding. A superimposed view of the AspH-WT and D721A $Fe(IV)=O$ complexes is shown in Fig. S49 in the ESI.†

The non-canonical water coordination to the non-heme $Fe(II)$ center (instead of carboxylate as in the canonical $Fe(II)/2OG$ enzymes) elevates the role of the interactions with the SCS. The hydrogen bond between the coordinated water molecule and the SCS residue Asp721 plays a key role in the reactivity of AspH compensating for the absence of coordinated carboxylate. Indeed, in agreement with earlier experimental studies which demonstrate that the mutation of D721A sharply decreases the enzyme activity,[195] our QM/MM study reveals that this mutation leads to an increased distance of 6.43 Å between the ferryl oxygen ($O_p$) and the $Asp103_{hFx}$ pro-*R* hydrogen atom (compared to 3.34 Å in the WT), and consequently to much higher energy barrier of 86.1 kcal mol$^{-1}$ (Fig. S50†). Such SCS carboxylate is unique for AspH and is not present in other $Fe(II)/2OG$ enzymes such as FIH, prolyl hydroxylase, and TauD where mutation of the Fe-coordinated carboxylate inactivates the enzymes.[85,88,234] Such SCS carboxylate is also missing in other $Fe(II)/2OG$ enzymes containing canonical facial triads such as PHF8,[196] KDM4A,[235] KDM2A,[236] ALKBH2 [237] and EFE.[133]

We further performed *in silico* mutation of the SCS residues Arg688 and Lys666, identified as crucial for TS stabilization and substrate binding, to alanine (A). The subsequent MD and QM/MM studies reveal that these SCS mutations (R688A and K666A) significantly change the productive orientation of the $Fe(IV)=O$ ES complex (Fig. S49 and S51†). The mutant forms show an increased distance between the $O_p$ and the $C_B$ atom of $Asp103_{hFX}$ compared to that in the WT. The average distances between the $O_p$ and the $C_B$ atom are 5.70 Å and 6.24 Å for R688A and K666A, respectively in comparison to 4.25 Å in the WT. Similarly, the angle between $Fe-O_p-C_B$ shows average values of 142.6° (R688A) and 147.4° (K666A) compared to 157.7° in the WT. The subsequent QM/MM studies of the mutant forms show that the increased distance significantly enhances the barrier for HAT (Fig. S52†). Our findings highlight these SCS residues' key role in proper substrate orientation, enabling productive catalysis, and providing insights into potential target residues for enzyme redesign and for altering substrate specificity.

## Conclusions

In conclusion, our study informs on the chemistry of the catalytic mechanism of the biologically and synthetically important 2OG-dependent dioxygenase AspH. Instead of using the characteristic HXD/EH facial triad, AspH replaces the carboxylate ligand with a Fe-coordinated water molecule, the position of which is controlled by the sidechain of the SCS carboxylate residue Asp721, which is also critical in catalysis. Our findings demonstrate that of the two crystallographically observed substrate binding modes, only the one not coordinating with the iron is catalytically active, as substrate coordination impedes the formation of the essential $Fe(IV)=O$ intermediate. The non-catalytically observed substrate carboxylate binding mode may help promote/stabilize iron binding in the absence of an enzyme supported carboxylate ligand. HAT is exothermic and occurs by σ channel mechanism. Atypically, rebound hydroxylation has a higher barrier than HAT, suggesting the rebound step could be the rate-limiting in AspH. HAT step and SCS residues (Arg688, Gln664, Lys666, Arg686, Asp721) enable stereoselective hydroxylation, highlighting the significance of SCS processes in promoting efficient catalysis and controlling the stereoselectivity in AspH. The TPR domain of AspH plays a significant role in EGFD substrate binding. It manifests dynamic motions during the catalysis which are of interest concerning the role of TPR domains in other 2OG oxygenases. The uncovered catalytic strategy of AspH provides novel insights for advancing the synthetic applications of $Fe(II)/2OG$ enzymes for regio- and stereoselective C–H bond functionalizations in biotechnology. The study affirms the roles of dynamics, SCS, and LR interactions as essential factors affecting catalysis and as potentially exciting tools for optimizing and redesigning enzymes for desired industrial applications. Our findings have implications for enzyme redesign, the development

of selective AspH inhibitors, and the advancement of regio- and stereoselective biocatalysis catalysts for C–H activation reactions.

## Data availability

The data supporting this study's findings are available from the corresponding author upon reasonable request.

## Author contributions

Conceptualization, T. G. K.-C.; methodology, T. G. K.-C. and A. K.; investigation and formal analysis, A. K. and S. O. W.; writing-original draft, A. K. and T. G. K.-C.; writing-review and editing, A. K., S. O. W., A. V., F. H. C., C. J. S., T. G. K.-C.; visualization, A. K.; funding acquisition, T. G. K.-C.; supervision, T. G. K.-C.

## Conflicts of interest

There are no conflicts to declare.

## Acknowledgements

## References

1 G. Zurlo, J. Guo, M. Takada, W. Wei and Q. Zhang, *Biochim. Biophys. Acta - Rev. Cancer*, 2016, **1866**, 208–220.

2 R. A. Berg and D. J. Prockop, *Biochem. Biophys. Res. Commun.*, 1973, **52**, 115–120.

3 K. L. Gorres and R. T. Raines, *Crit. Rev. Biochem. Mol. Biol.*, 2010, **45**, 106–124.

4 J. B. Hedges and K. S. Ryan, *Chem. Rev.*, 2020, **120**, 3161–3209.

5 C. T. Walsh, R. V. O'Brien and C. Khosla, *Angew. Chem., Int. Ed.*, 2013, **52**, 7098–7124.

6 R. Ushimaru and I. Abe, *ACS Catal.*, 2023, **13**, 1045–1076.

7 L.-F. Wu, S. Meng and G.-L. Tang, *Biochim. Biophys. Acta, Proteins Proteomics*, 2016, **1864**, 453–470.

8 C. R. Zwick III and H. Renata, *ACS Catal.*, 2023, **13**, 4853–4865.

9 N. Masson and P. J. Ratcliffe, *J. Cell Sci.*, 2003, **116**, 3041–3049.

10 D. Lando, D. J. Peet, J. J. Gorman, D. A. Whelan, M. L. Whitelaw and R. K. Bruick, *Genes Dev.*, 2002, **16**, 1466–1471.

11 A. K. Ohlin, G. Landes, P. Bourdon, C. Oppenheimer, R. Wydro and J. Stenflo, *J. Biol. Chem.*, 1988, **263**, 19240–19248.

12 J. M. Greve, A. M. Pinkham and J. A. Cowan, *Metallomics*, 2021, **13**, mfab044.

13 P. Fernlund and J. Stenflo, *J. Biol. Chem.*, 1983, **258**, 12509–12512.

14 J. Stenflo, A. Lundwall and B. Dahlback, *Proc. Natl. Acad. Sci. U. S. A.*, 1987, **84**, 368–372.

15 J. Stenflo, E. Holme, S. Lindstedt, N. Chandramouli, L. H. Huang, J. P. Tam and R. B. Merrifield, *Proc. Natl. Acad. Sci. U. S. A.*, 1989, **86**, 444–447.

16 J. E. Dinchuk, R. J. Focht, J. A. Kelley, N. L. Henderson, N. I. Zolotarjova, R. Wynn, N. T. Neff, J. Link, R. M. Huber, T. C. Burn, M. J. Rupar, M. R. Cunningham, B. H. Selling, J. Ma, A. A. Stern, G. F. Hollis, R. B. Stein and P. A. Friedman, *J. Biol. Chem.*, 2002, **277**, 12970–12977.

17 C. Loenarz and C. J. Schofield, *Trends Biochem. Sci.*, 2011, **36**, 7–18.

18 R. Jorissen, *Exp. Cell Res.*, 2003, **284**, 31–53.

19 P. Wee and Z. Wang, *Cancers*, 2017, **9**, 52.

20 N. Prenzel, O. M. Fischer, S. Streit, S. Hart and A. Ullrich, *Endocr. Relat. Cancer*, 2001, 11–31.

21 M. H. H. Schmidt, F. Bicker, I. Nikolic, J. Meister, T. Babuke, S. Picuric, W. Müller-Esterl, K. H. Plate and I. Dikic, *Nat. Cell Biol.*, 2009, **11**, 873–880.

22 D. P. Reinhardt, R. N. Ono, H. Notbohm, P. K. Müller, H. P. Bächinger and L. Y. Sakai, *J. Biol. Chem.*, 2000, **275**, 12339–12345.

23 R. W. Glanville, R. Q. Qian, D. W. McClure and C. L. Maslen, *J. Biol. Chem.*, 1994, **269**, 26630–26634.

24 H. Tran, W. J. VanDusen and W. S. Argraves, *J. Biol. Chem.*, 1997, **272**, 22600–22606.

25 C. M. Cardy and P. A. Handford, *J. Mol. Biol.*, 1998, **276**, 855–860.

26 J. Engel, *FEBS Lett.*, 1989, **251**, 1–7.

27 R. Timpl, T. Sasaki, G. Kostka and M.-L. Chu, *Nat. Rev. Mol. Cell Biol.*, 2003, **4**, 479–489.

28 F. Deák, R. Wagener, I. Kiss and M. Paulsson, *Matrix Biol.*, 1999, **18**, 55–64.

29 K. Godula and D. Sames, *Science*, 2006, **312**, 67–72.

30 J. Yamaguchi, A. D. Yamaguchi and K. Itami, *Angew. Chem., Int. Ed.*, 2012, **51**, 8960–9009.

31 L. Guillemard, N. Kaplaneris, L. Ackermann and M. J. Johansson, *Nat. Rev. Chem*, 2021, **5**, 522–545.

32 T. Rogge, N. Kaplaneris, N. Chatani, J. Kim, S. Chang, B. Punji, L. L. Schafer, D. G. Musaev, J. Wencel-Delord, C. A. Roberts, R. Sarpong, Z. E. Wilson, M. A. Brimble, M. J. Johansson and L. Ackermann, *Nat. Rev. Methods Primers*, 2021, **1**, 43.

33 K. Liao, T. C. Pickel, V. Boyarskikh, J. Bacsa, D. G. Musaev and H. M. L. Davies, *Nature*, 2017, **551**, 609–613.

34 T. Dalton, T. Faber and F. Glorius, *ACS Cent. Sci.*, 2021, **7**, 245–261.

35 J. Wencel-Delord, T. Dröge, F. Liu and F. Glorius, *Chem. Soc. Rev.*, 2011, **40**, 4740.

36 Y.-F. Liang and N. Jiao, *Acc. Chem. Res.*, 2017, **50**, 1640–1653.

37 S. Chakrabarty, Y. Wang, J. C. Perkins and A. R. H. Narayan, *Chem. Soc. Rev.*, 2020, **49**, 8137–8155.

38 J. C. Lewis, P. S. Coelho and F. H. Arnold, *Chem. Soc. Rev.*, 2011, **40**, 2003–2021.

39 R. K. Zhang, X. Huang and F. H. Arnold, *Curr. Opin. Chem. Biol.*, 2019, **49**, 67–75.

40 Y. Nakano, K. F. Biegasiewicz and T. K. Hyster, *Curr. Opin. Chem. Biol.*, 2019, **49**, 16–24.

41 F. Li, X. Zhang and H. Renata, *Curr. Opin. Chem. Biol.*, 2019, **49**, 25–32.

42 X. Ren and R. Fasan, *Curr. Opin. Green Sustain. Chem.*, 2021, **31**, 100494.

43 E. L. Bell, W. Finnigan, S. P. France, A. P. Green, M. A. Hayes, L. J. Hepworth, S. L. Lovelock, H. Niikura, S. Osuna, E. Romero, K. S. Ryan, N. J. Turner and S. L. Flitsch, *Nat. Rev. Methods Primers*, 2021, **1**, 46.

44 S. Kille, F. E. Zilly, J. P. Acevedo and M. T. Reetz, *Nat. Chem.*, 2011, **3**, 738–743.

45 S. M. Pratter, C. Konstantinovics, C. M. L. Di Giuro, E. Leitner, D. Kumar, S. P. de Visser, G. Grogan and G. D. Straganz, *Angew. Chem., Int. Ed.*, 2013, **52**, 9677–9681.

46 M. D. Toscano, K. J. Woycechowsky and D. Hilvert, *Angew. Chem., Int. Ed.*, 2007, **46**, 3212–3236.

47 F. Schwizer, Y. Okamoto, T. Heinisch, Y. Gu, M. M. Pellizzoni, V. Lebrun, R. Reuter, V. Köhler, J. C. Lewis and T. R. Ward, *Chem. Rev.*, 2018, **118**, 142–231.

48 H. J. Davis and T. R. Ward, *ACS Cent. Sci.*, 2019, **5**, 1120–1136.

49 K. Chen and F. H. Arnold, *Nat. Catal.*, 2020, **3**, 203–213.

50 V. Steck, J. N. Kolev, X. Ren and R. Fasan, *J. Am. Chem. Soc.*, 2020, **142**, 10343–10357.

51 D. Mondal, H. M. Snodgrass, C. A. Gomez and J. C. Lewis, *Chem. Rev.*, 2023, **123**, 10381–10431.

52 N. P. Dunham and F. H. Arnold, *ACS Catal.*, 2020, **10**, 12239–12255.

53 J. Lee and N. M. Goodey, *Chem. Rev.*, 2011, **111**, 7595–7624.

54 J. C. Lewis, *Acc. Chem. Res.*, 2019, **52**, 576–584.

55 C. Van Stappen, Y. Deng, Y. Liu, H. Heidari, J.-X. Wang, Y. Zhou, A. P. Ledray and Y. Lu, *Chem. Rev.*, 2022, **122**, 11974–12045.

56 S. T. Stripp, B. R. Duffus, V. Fourmond, C. Léger, S. Leimkühler, S. Hirota, Y. Hu, A. Jasniewski, H. Ogata and M. W. Ribbe, *Chem. Rev.*, 2022, **122**, 11900–11973.

57 S. S. Chaturvedi, S. B. Jaber Sathik Rifayee, S. O. Waheed, J. Wildey, C. Warner, C. J. Schofield, T. G. Karabencheva-Christova and C. Z. Christov, *JACS Au*, 2022, **2**, 2169–2186.

58 S. P. Visser, *Chem. –Euro. J.*, 2020, **26**, 5308–5327.

59 R. H. Wilson, S. Chatterjee, E. R. Smithwick, J. J. Dalluge and A. Bhagi-Damodaran, *ACS Catal.*, 2022, **12**, 10913–10924.

60 C. Peters and R. Buller, *Catalysts*, 2019, **9**, 221.

61 R. S. Gronke, W. J. VanDusen, V. M. Garsky, J. W. Jacobs, M. K. Sardana, A. M. Stern and P. A. Friedman, *Proc. Natl. Acad. Sci. U. S. A.*, 1989, **86**, 3609–3613.

62 I. Pfeffer, L. Brewitz, T. Krojer, S. A. Jensen, G. T. Kochan, N. J. Kershaw, K. S. Hewitson, L. A. McNeill, H. Kramer, M. Münzel, R. J. Hopkinson, U. Oppermann, P. A. Handford, M. A. McDonough and C. J. Schofield, *Nat. Commun.*, 2019, **10**, 1–16.

63 Md. S. Islam, T. M. Leissing, R. Chowdhury, R. J. Hopkinson and C. J. Schofield, *Annu. Rev. Biochem.*, 2018, **87**, 585–620.

64 L. Brewitz, B. C. Onisko and C. J. Schofield, *J. Biol. Chem.*, 2022, **298**, 102129.

65 F. Gundogan, A. Bedoya, J. Gilligan, E. Lau, P. Mark, M. E. De Paepe and S. M. De la Monte, *Pathol. Res. Pract.*, 2011, **207**, 545–553.

66 F. Gundogan, J. Gilligan, W. Qi, E. Chen, R. Naram and S. M. De La Monte, *Placenta*, 2015, **36**, 523–530.

67 S. Shawaf, B. Noureddin, A. Khouri and E. I. Traboulsi, *Ophthalmic Genet.*, 1995, **16**, 163–169.

68 R. Haddad, S. Uwaydat, R. Dakroub and E. I. Traboulsi, *Am. J. Med. Genet.*, 2001, **99**, 185–189.

69 N. Patel, A. O. Khan, A. Mansour, J. Y. Mohamed, A. Al-Assiri, R. Haddad, X. Jia, Y. Xiong, A. Mégarbané, E. I. Traboulsi and F. S. Alkuraya, *Am. J. Hum. Genet.*, 2014, **94**, 755–759.

70 C. Lei, T. Guo, S. Ding, L. Liao, H. Peng, Z. Tan and H. Luo, *Mol. Genet. Genomic Med.*, 2021, **9**, 1–8.

71 M. Kanwal, M. Smahel, M. Olsen, J. Smahelova and R. Tachezy, *J. Exp. Clin. Cancer Res.*, 2020, **39**, 163.

72 G. Hou, B. Xu, Y. Bi, C. Wu, B. Ru, B. Sun and X. Bai, *Bosn. J. Basic Med. Sci.*, 2018, **18**, 297–304.

73 R. Benelli, D. Costa, L. Mastracci, F. Grillo, M. J. Olsen, P. Barboro, A. Poggi and N. Ferrari, *Cancers*, 2020, **12**, 971.

74 L. Brewitz, A. Tumber, I. Pfeffer, M. A. McDonough and C. J. Schofield, *Sci. Rep.*, 2020, **10**, 8650.

75 L. Brewitz, A. Tumber and C. J. Schofield, *J. Biol. Chem.*, 2020, **295**, 7826–7838.

76 Y. Mao, W. Zhang, Z. Fu, Y. Liu, L. Chen, X. Lian, D. Zhuo, J. Wu, M. Zheng and C. Liao, *Angew. Chem., Int. Ed.*, 2023, **62**, e202305250.

77 L. Que and R. Y. N. Ho, *Chem. Rev.*, 1996, **96**, 2607–2624.

78 E. L. Hegg and L. Q. Jr, *Eur. J. Biochem.*, 1997, **250**, 625–629.

79 L. Que, *Nat. Struct. Mol. Biol.*, 2000, **7**, 182–184.

80 A. Bassan, T. Borowski and P. E. M. Siegbahn, *Dalton Trans.*, 2004, **20**, 3153–3162.

81 A. Brasnett, I. Pfeffer, L. Brewitz, R. Chowdhury, Y. Nakashima, A. Tumber, M. A. McDonough and C. J. Schofield, *Angew. Chem., Int. Ed.*, 2021, **60**, 14657–14663.

82 M. Ueki, D. P. Galonić, F. H. Vaillancourt, S. Garneau-Tsodikova, E. Yeh, D. A. Vosburg, F. C. Schroeder, H. Osada and C. T. Walsh, *Chem. Biol.*, 2006, **13**, 1183–1191.

83 L. C. Blasiak, F. H. Vaillancourt, C. T. Walsh and C. L. Drennan, *Nature*, 2006, **440**, 368–371.

84 L. C. Blasiak and C. L. Drennan, *Acc. Chem. Res.*, 2009, **42**, 147–155.

85 K. S. Hewitson, S. L. Holmes, D. Ehrismann, A. P. Hardy, R. Chowdhury, C. J. Schofield and M. A. McDonough, *J. Biol. Chem.*, 2008, **283**, 25971–25978.

86 M. L. Neidig, C. D. Brown, K. M. Light, D. G. Fujimori, E. M. Nolan, J. C. Price, E. W. Barr, J. M. Bollinger, C. Krebs, C. T. Walsh and E. I. Solomon, *J. Am. Chem. Soc.*, 2007, **129**, 14224–14231.

87 S. R. Iyer, V. D. Chaplin, M. J. Knapp and E. I. Solomon, *J. Am. Chem. Soc.*, 2018, **140**, 11777–11783.

88 K. L. Gorres, K. H. Pua and R. T. Raines, *PLoS One*, 2009, **4**, e7635.

89 G. L. Blatch and M. Lässle, *BioEssays*, 1999, **21**, 932–939.

90  W. Aik, M. A. McDonough, A. Thalhammer, R. Chowdhury and C. J. Schofield, *Curr. Opin. Struct. Biol.*, 2012, **22**, 691–700.

91  I. J. Clifton, M. A. McDonough, D. Ehrismann, N. J. Kershaw, N. Granatino and C. J. Schofield, *J. Inorg. Biochem.*, 2006, **100**, 644–669.

92  M. Pekkala, R. Hieta, U. Bergmann, K. I. Kivirikko, R. K. Wierenga and J. Myllyharju, *J. Biol. Chem.*, 2004, **279**, 52255–52261.

93  M. K. Koski, R. Hieta, M. Hirsilä, A. Rönkä, J. Myllyharju and R. K. Wierenga, *J. Biol. Chem.*, 2009, **284**, 25290–25301.

94  P. J. Pollard, C. Loenarz, D. R. Mole, M. A. McDonough, J. M. Gleadle, C. J. Schofield and P. J. Ratcliffe, *Biochem. J.*, 2008, **416**, 387–394.

95  R. Chowdhury, R. Sekirnik, N. C. Brissett, T. Krojer, C. Ho, S. S. Ng, I. J. Clifton, W. Ge, N. J. Kershaw, G. C. Fox, J. R. C. Muniz, M. Vollmar, C. Phillips, E. S. Pilka, K. L. Kavanagh, F. Von Delft, U. Oppermann, M. A. McDonough, A. J. Doherty and C. J. Schofield, *Nature*, 2014, **510**, 422–426.

96  D. Petrović, V. A. Risso, S. C. L. Kamerlin and J. M. Sanchez-Ruiz, *J. R. Soc. Interface*, 2018, **15**, 20180330.

97  B. J. Bahnson, T. D. Colby, J. K. Chin, B. M. Goldstein and J. P. Klinman, *Proc. Natl. Acad. Sci. U. S. A.*, 1997, **94**, 12797–12802.

98  R. B. Leveson-Gower, C. Mayer and G. Roelfes, *Nat. Rev. Chem*, 2019, **3**, 687–705.

99  S. O. Waheed, R. Ramanan, S. S. Chaturvedi, J. Ainsley, M. Evison, J. M. Ames, C. J. Schofield, C. Z. Christov and T. G. Karabencheva-Christova, *Org. Biomol. Chem.*, 2019, **17**, 2223–2231.

100 S. S. Chaturvedi, R. Ramanan, S. O. Waheed, J. Ainsley, M. Evison, J. M. Ames, C. J. Schofield, T. G. Karabencheva-Christova and C. Z. Christov, *Chem. –Euro. J.*, 2019, **25**, 5422–5426.

101 R. P. Hausinger, *Crit. Rev. Biochem. Mol. Biol.*, 2004, **39**, 21–68.

102 S. Martinez and R. P. Hausinger, *J. Biol. Chem.*, 2015, **290**, 20702–20711.

103 E. G. Kovaleva and J. D. Lipscomb, *Science*, 2007, **316**, 453–457.

104 P. K. Grzyska, E. H. Appelman, R. P. Hausinger and D. A. Proshlyakov, *Proc. Natl. Acad. Sci. U. S. A.*, 2010, **107**, 3982–3987.

105 H. M. Hanauske-Abel and V. Günzler, *J. Theor. Biol.*, 1982, **94**, 421–455.

106 E. I. Solomon, S. Goudarzi and K. D. Sutherlin, *Biochemistry*, 2016, **55**, 6363–6374.

107 N. Lehnert and E. I. Solomon, *J. Biol. Inorg. Chem.*, 2003, **8**, 294–305.

108 E. I. Solomon, K. M. Light, L. V. Liu, M. Srnec and S. D. Wong, *Acc. Chem. Res.*, 2013, **46**, 2725–2739.

109 E. I. Solomon, S. D. Wong, L. V. Liu, A. Decker and M. S. Chow, *Curr. Opin. Chem. Biol.*, 2009, **13**, 99–113.

110 T. Borowski, H. Noack, M. Radoń, K. Zych and P. E. M. Siegbahn, *J. Am. Chem. Soc.*, 2010, **132**, 12887–12898.

111 S. D. Wong, M. Srnec, M. L. Matthews, L. V. Liu, Y. Kwak, K. Park, C. B. Bell Iii, E. E. Alp, J. Zhao, Y. Yoda, S. Kitao, M. Seto, C. Krebs, J. M. Bollinger and E. I. Solomon, *Nature*, 2013, **499**, 320–323.

112 H. J. Kulik and C. L. Drennan, *J. Biol. Chem.*, 2013, **288**, 11233–11241.

113 M. G. Quesne, R. Latifi, L. E. Gonzalez-Ovalle, D. Kumar and S. P. de Visser, *Chem. –Euro. J.*, 2014, **20**, 435–446.

114 A. Timmins, M. Saint-André and S. P. De Visser, *J. Am. Chem. Soc.*, 2017, **139**, 9855–9866.

115 K.-B. Cho, H. Hirao, S. Shaik and W. Nam, *Chem. Soc. Rev.*, 2016, **45**, 1197–1210.

116 J. Zhang, P. Wu, X. Zhang and B. Wang, *ChemBioChem*, 2023, **24**, e202300119.

117 W. Singh, D. Quinn, T. S. Moody and M. Huang, *J. Phys. Chem. B*, 2019, **123**, 7801–7811.

118 J. Li, H.-J. Liao, Y. Tang, J.-L. Huang, L. Cha, T.-S. Lin, J. L. Lee, I. V. Kurnikov, M. G. Kurnikova, W. Chang, N.-L. Chan and Y. Guo, *J. Am. Chem. Soc.*, 2020, **142**, 6268–6284.

119 J. Xue, J. Lu and W. Lai, *Phys. Chem. Chem. Phys.*, 2019, **21**, 9957–9968.

120 S. P. de Visser, *Chem. Rec.*, 2018, **18**, 1501–1516.

121 S. O. Waheed, R. Ramanan, S. S. Chaturvedi, N. Lehnert, C. J. Schofield, C. Z. Christov and T. G. Karabencheva-Christova, *ACS Cent. Sci.*, 2020, **6**, 795–814.

122 S. S. Chaturvedi, R. Ramanan, N. Lehnert, C. J. Schofield, T. G. Karabencheva-Christova and C. Z. Christov, *ACS Catal.*, 2020, **10**, 1195–1209.

123 R. Ramanan, S. S. Chaturvedi, N. Lehnert, C. J. Schofield, T. G. Karabencheva-Christova and C. Z. Christov, *Chem. Sci.*, 2020, **11**, 9950–9961.

124 M. M. Mbughuni, M. Chakrabarti, J. A. Hayden, E. L. Bominaar, M. P. Hendrich, E. Münck and J. D. Lipscomb, *Proc. Natl. Acad. Sci. U. S. A.*, 2010, **107**, 16788–16793.

125 J. C. Price, E. W. Barr, T. E. Glass, C. Krebs and J. M. Bollinger, *J. Am. Chem. Soc.*, 2003, **125**, 13008–13009.

126 C. Krebs, D. Galonić Fujimori, C. T. Walsh and J. Martin Bollinger Jr, *Acc. Chem. Res.*, 2007, **40**, 484–492.

127 E. I. Solomon, D. E. DeWeese and J. T. Babicz Jr, *Biochemistry*, 2021, **60**, 3497–3506.

128 P. J. Riggs-Gelasco, J. C. Price, R. B. Guyer, J. H. Brehm, E. W. Barr, J. M. Bollinger and C. Krebs, *J. Am. Chem. Soc.*, 2004, **126**, 8108–8109.

129 J. C. Price, E. W. Barr, B. Tirupati, J. M. Bollinger and C. Krebs, *Biochemistry*, 2003, **42**, 7497–7508.

130 M. Srnec, S. D. Wong, M. L. Matthews, C. Krebs, J. M. Bollinger and E. I. Solomon, *J. Am. Chem. Soc.*, 2016, **138**, 5110–5122.

131 M. L. Neidig, A. Decker, O. W. Choroba, F. Huang, M. Kavana, G. R. Moran, J. B. Spencer and E. I. Solomon, *Proc. Natl. Acad. Sci. U. S. A.*, 2006, **103**, 12966–12973.

132 P. Rabe, J. J. A. G. Kamps, K. D. Sutherlin, J. D. S. Linyard, P. Aller, C. C. Pham, H. Makita, I. Clifton, M. A. McDonough, T. M. Leissing, D. Shutin, P. A. Lang, A. Butryn, J. Brem, S. Gul, F. D. Fuller, I.-S. Kim,

M. H. Cheah, T. Fransson, A. Bhowmick, I. D. Young, L. O'Riordan, A. S. Brewster, I. Pettinati, M. Doyle, Y. Joti, S. Owada, K. Tono, A. Batyuk, M. S. Hunter, R. Alonso-Mori, U. Bergmann, R. L. Owen, N. K. Sauter, T. D. W. Claridge, C. V. Robinson, V. K. Yachandra, J. Yano, J. F. Kern, A. M. Orville and C. J. Schofield, *Sci. Adv.*, 2021, **7**, eabh0250.

133 S. Martinez, M. Fellner, C. Q. Herr, A. Ritchie, J. Hu and R. P. Hausinger, *J. Am. Chem. Soc.*, 2017, **139**, 11980–11988.

134 L. Hu, Z. Li, J. Cheng, Q. Rao, W. Gong, M. Liu, Y. G. Shi, J. Zhu, P. Wang and Y. Xu, *Cell*, 2013, **155**, 1545–1555.

135 I. Zoi, J. Suarez, D. Antoniou, S. A. Cameron, V. L. Schramm and S. D. Schwartz, *J. Am. Chem. Soc.*, 2016, **138**, 3403–3409.

136 S. S. Chaturvedi, R. Ramanan, J. Hu, R. P. Hausinger and C. Z. Christov, *ACS Catal.*, 2021, **11**, 1578–1592.

137 R. Mehmood, H. W. Qi, A. H. Steeves and H. J. Kulik, *ACS Catal.*, 2019, **9**, 4930–4943.

138 S. O. Waheed, S. S. Chaturvedi, T. G. Karabencheva-Christova and C. Z. Christov, *ACS Catal.*, 2021, **11**, 3877–3890.

139 Z. Wojdyla and T. Borowski, *Chem. –Euro. J.*, 2022, **28**, e202104106.

140 A. Šali and T. L. Blundell, *J. Mol. Biol.*, 1993, **234**, 779–815.

141 A. Fiser and A. Šali, *Methods Enzymol.*, 2003, **374**, 461–491.

142 M. H. M. Olsson, C. R. Søndergaard, M. Rostkowski and J. H. Jensen, *J. Chem. Theory Comput.*, 2011, **7**, 525–537.

143 P. Li and K. M. Merz, *J. Chem. Inf. Model.*, 2016, **56**, 599–604.

144 D. A. Case, K. Belfon, I. Y. Ben-Shalom, S. R. Brozell, D. S. Cerutti, T. E. Cheatham III, V. W. D. Cruzeiro, T. A. Darden, R. E. Duke, G. Giambasu, M. K. Gilson, H. Gohlke, A. W. Goetz, R. Harris, S. Izadi, S. A. Izmailov, K. Kasavajhala, A. Kovalenko, R. Krasny, T. Kurtzman, T. S. Lee, S. LeGrand, P. Li, C. Lin, J. Liu, T. Luchko, R. Luo, V. Man, K. M. Merz, Y. Miao, O. Mikhailovskii, G. Monard, H. Nguyen, A. Onufriev, F. Pan, S. Pantano, R. Qi, D. R. Roe, A. Roitberg, C. Sagui, S. Schott-Verdugo, J. Shen, C. L. Simmerling, N. R. Skrynnikov, J. Smith, J. Swails, R. C. Walker, J. Wang, L. Wilson, R. M. Wolf, X. Wu, Y. Xiong, Y. Xue, D. M. York and P. A. Kollman, *AMBER 2020*, University of California, San Francisco, 2020.

145 J. M. Seminario, *Int. J. Quantum Chem.*, 1996, **60**, 1271–1277.

146 R. J. Woods and R. Chappelle, *J. Mol. Struct.*, 2000, **527**, 149–156.

147 J. Wang, W. Wang, P. A. Kollman and D. A. Case, *J. Mol. Graph.*, 2006, **25**, 247–260.

148 W. L. Jorgensen, J. Chandrasekhar, J. D. Madura, R. W. Impey and M. L. Klein, *J. Chem. Phys.*, 1983, **79**, 926–935.

149 A. Pabis, I. Geronimo, D. M. York and P. Paneth, *J. Chem. Theory Comput.*, 2014, **10**, 2246–2254.

150 R. L. Davidchack, T. E. Ouldridge and M. V. Tretyakov, *J. Chem. Phys.*, 2015, **142**, 144114.

151 J. A. Maier, C. Martinez, K. Kasavajhala, L. Wickstrom, K. E. Hauser and C. Simmerling, *J. Chem. Theory Comput.*, 2015, **11**, 3696–3713.

152 F. Bresme, *J. Chem. Phys.*, 2001, **115**, 7564–7574.

153 J.-P. Ryckaert, G. Ciccotti and H. J. C. Berendsen, *J. Comput. Phys.*, 1977, **23**, 327–341.

154 M. Deserno and C. Holm, *J. Chem. Phys.*, 1998, **109**, 7678–7693.

155 D. R. Roe and T. E. Cheatham, *J. Chem. Theory Comput.*, 2013, **9**, 3084–3095.

156 W. Humphrey, A. Dalke and K. Schulten, *J. Mol. Graph.*, 1996, **14**, 33–38.

157 E. F. Pettersen, T. D. Goddard, C. C. Huang, G. S. Couch, D. M. Greenblatt, E. C. Meng and T. E. Ferrin, *J. Comput. Chem.*, 2004, **25**, 1605–1612.

158 B. J. Grant, A. P. C. Rodrigues, K. M. ElSawy, J. A. McCammon and L. S. D. Caves, *Bioinformatics*, 2006, **22**, 2695–2696.

159 D. Bakowies and W. Thiel, *J. Phys. Chem.*, 1996, **100**, 10580–10594.

160 S. Metz, J. Kästner, A. A. Sokol, T. W. Keal and P. Sherwood, *Wiley Interdiscip. Rev.: Comput. Mol. Sci.*, 2014, **4**, 101–110.

161 R. Ahlrichs, M. Bär, M. Häser, H. Horn and C. Kölmel, *Chem. Phys. Lett.*, 1989, **162**, 165–169.

162 W. Smith and T. R. Forester, *J. Mol. Graph.*, 1996, **14**, 136–141.

163 U. C. Singh and P. A. Kollman, *J. Comput. Chem.*, 1986, **7**, 718–730.

164 M. J. Field, P. A. Bash and M. Karplus, *J. Comput. Chem.*, 1990, **11**, 700–733.

165 P. Sherwood, A. H. De Vries, M. F. Guest, G. Schreckenbach, C. R. A. Catlow, S. A. French, A. A. Sokol, S. T. Bromley, W. Thiel, A. J. Turner, S. Billeter, F. Terstegen, S. Thiel, J. Kendrick, S. C. Rogers, J. Casci, M. Watson, F. King, E. Karlsen, M. Sjøvoll, A. Fahmi, A. Schäfer and C. Lennartz, *J. Mol. Struct.*, 2003, **632**, 1–28.

166 J. Kästner, J. M. Carr, T. W. Keal, W. Thiel, A. Wander and P. Sherwood, *J. Phys. Chem. A*, 2009, **113**, 11856–11865.

167 G. Henkelman and H. Jónsson, *J. Chem. Phys.*, 1999, **111**, 7010–7022.

168 S. Grimme, *J. Comput. Chem.*, 2004, **25**, 1463–1473.

169 S. Grimme, *J. Comput. Chem.*, 2006, **27**, 1787–1799.

170 S. Grimme, J. Antony, S. Ehrlich and H. Krieg, *J. Chem. Phys.*, 2010, **132**, 154104.

171 F. Sheong, J.-X. Zhang and Z. Lin, *J. Comput. Chem.*, 2019, **40**, 1172–1184.

172 T. Stuyver, J. Huang, D. Mallick, D. Danovich and S. Shaik, *J. Comput. Chem.*, 2020, **41**, 74–82.

173 S. E. Graham, F. Syeda and G. A. Cisneros, *Biochemistry*, 2012, **51**, 2569–2578.

174 S. W. Dewage and G. A. Cisneros, *J. Phys. Chem. B*, 2015, **119**, 3669–3677.

175 H. Torabifard and G. A. Cisneros, *Chem. Sci.*, 2018, **9**, 8433–8445.

176 M. J. Frisch, G. W. Trucks, H. B. Schlegel, G. E. Scuseria, M. A. Robb, J. R. Cheeseman, G. Scalmani, V. Barone, G. A. Petersson, H. Nakatsuji, X. Li, M. Caricato, A. V. Marenich, J. Bloino, B. G. Janesko, R. Gomperts, B. Mennucci, H. P. Hratchian, J. V. Ortiz, A. F. Izmaylov, J. L. Sonnenberg, D. Williams-Young, F. Ding, F. Lipparini, F. Egidi, J. Goings, B. Peng, A. Petrone,

T. Henderson, D. Ranasinghe, V. G. Zakrzewski, J. Gao, N. Rega, G. Zheng, W. Liang, M. Hada, M. Ehara, K. Toyota, R. Fukuda, J. Hasegawa, M. Ishida, T. Nakajima, Y. Honda, O. Kitao, H. Nakai, T. Vreven, K. Throssell, J. A. Montgomery Jr, J. E. Peralta, F. Ogliaro, M. J. Bearpark, J. J. Heyd, E. N. Brothers, K. N. Kudin, V. N. Staroverov, T. A. Keith, R. Kobayashi, J. Normand, K. Raghavachari, A. P. Rendell, J. C. Burant, S. S. Iyengar, J. Tomasi, M. Cossi, J. M. Millam, M. Klene, C. Adamo, R. Cammi, J. W. Ochterski, R. L. Martin, K. Morokuma, O. Farkas, J. B. Foresman and D. J. Fox, *Gaussian 16 Rev. A.03*, 2016.

177 T. D. Kühne, M. Iannuzzi, M. Del Ben, V. V. Rybkin, P. Seewald, F. Stein, T. Laino, R. Z. Khaliullin, O. Schütt, F. Schiffmann, D. Golze, J. Wilhelm, S. Chulkov, M. H. Bani-Hashemian, V. Weber, U. Borštnik, M. Taillefumier, A. S. Jakobovits, A. Lazzaro, H. Pabst, T. Müller, R. Schade, M. Guidon, S. Andermatt, N. Holmberg, G. K. Schenter, A. Hehn, A. Bussy, F. Belleflamme, G. Tabacchi, A. Glöß, M. Lass, I. Bethune, C. J. Mundy, C. Plessl, M. Watkins, J. VandeVondele, M. Krack and J. Hutter, *J. Chem. Phys.*, 2020, **152**, 194103.

178 J. VandeVondele, M. Krack, F. Mohamed, M. Parrinello, T. Chassaing and J. Hutter, *Comput. Phys. Commun.*, 2005, **167**, 103–128.

179 A. Laio, J. VandeVondele and U. Rothlisberger, *J. Chem. Phys.*, 2002, **116**, 6941–6947.

180 T. Laino, F. Mohamed, A. Laio and M. Parrinello, *J. Chem. Theory Comput.*, 2005, **1**, 1176–1184.

181 J. VandeVondele and J. Hutter, *J. Chem. Phys.*, 2007, **127**, 114105.

182 S. Goedecker, M. Teter and J. Hutter, *Phys. Rev. B*, 1996, **54**, 1703–1710.

183 M. Guidon, J. Hutter and J. VandeVondele, *J. Chem. Theory Comput.*, 2010, **6**, 2348–2364.

184 M. Karplus and J. A. McCammon, *Nat. Struct. Mol. Biol.*, 2002, **9**, 646–652.

185 E. Z. Eisenmesser, D. A. Bosco, M. Akke and D. Kern, *Science*, 2002, **295**, 1520–1523.

186 M. Karplus and J. Kuriyan, *Proc. Natl. Acad. Sci. U. S. A.*, 2005, **102**, 6679–6685.

187 J. P. Klinman, *Acc. Chem. Res.*, 2015, **48**, 449–456.

188 A. G. Palmer, *Acc. Chem. Res.*, 2015, **48**, 457–465.

189 A. Kohen, *Acc. Chem. Res.*, 2015, **48**, 466–473.

190 G. Bhabha, J. T. Biel and J. S. Fraser, *Acc. Chem. Res.*, 2015, **48**, 423–430.

191 M. H. M. Olsson, W. W. Parson and A. Warshel, *Chem. Rev.*, 2006, **106**, 1737–1756.

192 S. S. Chaturvedi, R. Ramanan, S. O. Waheed, T. G. Karabencheva-Christova and C. Z. Christov, in *Advances in Protein Chemistry and Structural Biology*, Elsevier, 2019, vol. 117, pp. 113–125.

193 T. G. Karabencheva-Christova, C. Z. Christov and G. B. Fields, in *Advances in Protein Chemistry and Structural Biology*, Elsevier, 2017, vol. 109, pp. 1–24.

194 J. Ainsley, A. Lodola, A. J. Mulholland, C. Z. Christov and T. G. Karabencheva-Christova, in *Advances in Protein*

*Chemistry and Structural Biology*, Elsevier, 2018, vol. 113, pp. 1–32.

195 J. M. Greve, A. M. Pinkham, Z. Thompson and J. A. Cowan, *Metallomics*, 2021, **13**, mfab056.

196 J. R. Horton, A. K. Upadhyay, H. H. Qi, X. Zhang, Y. Shi and X. Cheng, *Nat. Struct. Mol. Biol.*, 2010, **17**, 38–43.

197 C. Lemay-St-Denis, N. Doucet and J. N. Pelletier, *Protein Eng. Des. Sel.*, 2022, **35**, gzac015.

198 M. C. C. J. C. Ebert, S. L. Dürr, A. A. Houle, G. Lamoureux and J. N. Pelletier, *ACS Catal.*, 2016, **6**, 7426–7437.

199 L. Alejaldre, C. Lemay-St-Denis, J. N. Pelletier and D. Quaglia, *Biochemistry*, 2023, **62**, 396–409.

200 M. B. Berger, A. R. Walker, E. A. Vázquez-Montelongo and G. A. Cisneros, *Phys. Chem. Chem. Phys.*, 2021, **23**, 22227–22240.

201 K. D. Dubey and S. Shaik, *Acc. Chem. Res.*, 2019, **52**, 389–399.

202 J. Huang, C. Li, B. Wang, D. A. Sharon, W. Wu and S. Shaik, *ACS Catal.*, 2016, **6**, 2694–2704.

203 S. O. Waheed, A. Varghese, I. DiCastri, B. Kaski, C. LaRouche, G. B. Fields and T. G. Karabencheva-Christova, *ChemPhysChem*, 2023, **24**, e202200649.

204 S. Shaik, H. Chen and D. Janardanan, *Nat. Chem.*, 2011, **3**, 19–27.

205 B. Wang, E. M. Johnston, P. Li, S. Shaik, G. J. Davies, P. H. Walton and C. Rovira, *ACS Catal.*, 2018, **8**, 1346–1351.

206 S. Ye and F. Neese, *Proc. Natl. Acad. Sci. U. S. A.*, 2011, **108**, 1228–1233.

207 S. Shaik, H. Hirao and D. Kumar, *Acc. Chem. Res.*, 2007, **40**, 532–542.

208 S. Ye, C. Riplinger, A. Hansen, C. Krebs, J. M. Bollinger and F. Neese, *Chem.–Euro. J.*, 2012, **18**, 6555–6567.

209 L. M. Mirica, K. P. McCusker, J. W. Munos, H. Liu and J. P. Klinman, *J. Am. Chem. Soc.*, 2008, **130**, 8122–8123.

210 I. A. Topol, A. V. Nemukhin, K. Salnikow, R. E. Cachau, Y. G. Abashkin, K. S. Kasprzak and S. K. Burt, *J. Phys. Chem. A*, 2006, **110**, 4223–4228.

211 J. A. Hangasky, H. Gandhi, M. A. Valliere, N. E. Ostrom and M. J. Knapp, *Biochemistry*, 2014, **53**, 8077–8084.

212 S. Goudarzi, S. R. Iyer, J. T. Babicz, J. J. Yan, G. H. J. Peters, H. E. M. Christensen, B. Hedman, K. O. Hodgson and E. I. Solomon, *Proc. Natl. Acad. Sci. U. S. A.*, 2020, **117**, 5152–5159.

213 J. Zhou, M. Gunsior, B. O. Bachmann, C. A. Townsend and E. I. Solomon, *J. Am. Chem. Soc.*, 1998, **120**, 13539–13540.

214 H. Liu, J. Llano and J. W. Gauld, *J. Phys. Chem. B*, 2009, **113**, 4887–4898.

215 C. Geng, S. Ye and F. Neese, *Angew. Chem., Int. Ed.*, 2010, **49**, 5717–5720.

216 D. Fang, R. L. Lord and G. A. Cisneros, *J. Phys. Chem. B*, 2013, **117**, 6410–6420.

217 S. O. Waheed, A. Varghese, S. S. Chaturvedi, T. G. Karabencheva-Christova and C. Z. Christov, *ACS Catal.*, 2022, **12**, 5327–5344.

218 S. P. De Visser, *J. Am. Chem. Soc.*, 2006, **128**, 9813–9824.

219 D. Usharani, D. Janardanan and S. Shaik, *J. Am. Chem. Soc.*, 2011, **133**, 176–179.

220 S. B. J. S. Rifayee, S. S. Chaturvedi, C. Warner, J. Wildey, W. White, M. Thompson, C. J. Schofield and C. Z. Christov, *Chem. –Euro. J.*, 2023, **29**, e202301305.

221 L. M. Hoffart, E. W. Barr, R. B. Guyer, J. M. Bollinger and C. Krebs, *Proc. Natl. Acad. Sci. U. S. A.*, 2006, **103**, 14738–14743.

222 D. W. Kastner, A. Nandy, R. Mehmood and H. J. Kulik, *ACS Catal.*, 2023, **13**, 2489–2501.

223 L. J. Walport, R. J. Hopkinson, R. Chowdhury, R. Schiller, W. Ge, A. Kawamura and C. J. Schofield, *Nat. Commun.*, 2016, **7**, 11974.

224 J. Lu, L. Hu, J. Cheng, D. Fang, C. Wang, K. Yu, H. Jiang, Q. Cui, Y. Xu and C. Luo, *Phys. Chem. Chem. Phys.*, 2016, **18**, 4728–4738.

225 F. Chen, K. Bian, Q. Tang, B. I. Fedeles, V. Singh, Z. T. Humulock, J. M. Essigmann and D. Li, *Chem. Res. Toxicol.*, 2017, **30**, 1102–1110.

226 A. Warshel, P. K. Sharma, M. Kato, Y. Xiang, H. Liu and M. H. M. Olsson, *Chem. Rev.*, 2006, **106**, 3210–3235.

227 W. Peng, S. Yan, X. Zhang, L. Liao, J. Zhang, S. Shaik and B. Wang, *J. Am. Chem. Soc.*, 2022, **144**, 20484–20494.

228 B. Wang, Z. Cao, D. A. Sharon and S. Shaik, *ACS Catal.*, 2015, **5**, 7077–7090.

229 P. Schyman, W. Lai, H. Chen, Y. Wang and S. Shaik, *J. Am. Chem. Soc.*, 2011, **133**, 7977–7984.

230 H. J. Kulik, L. C. Blasiak, N. Marzari and C. L. Drennan, *J. Am. Chem. Soc.*, 2009, **131**, 14426–14433.

231 M. Srnec and E. I. Solomon, *J. Am. Chem. Soc.*, 2017, **139**, 2396–2407.

232 A. Timmins, N. J. Fowler, J. Warwicker, G. D. Straganz and S. P. De Visser, *Front. Chem.*, 2018, **6**, 513.

233 E. I. Solomon, A. Decker and N. Lehnert, *Proc. Natl. Acad. Sci. U. S. A.*, 2003, **100**, 3589–3594.

234 P. K. Grzyska, T. A. Müller, M. G. Campbell and R. P. Hausinger, *J. Inorg. Biochem.*, 2007, **101**, 797–808.

235 S. S. Ng, K. L. Kavanagh, M. A. McDonough, D. Butler, E. S. Pilka, B. M. R. Lienard, J. E. Bray, P. Savitsky, O. Gileadi, F. Von Delft, N. R. Rose, J. Offer, J. C. Scheinost, T. Borowski, M. Sundstrom, C. J. Schofield and U. Oppermann, *Nature*, 2007, **448**, 87–91.

236 Z. Cheng, P. Cheung, A. J. Kuo, E. T. Yukl, C. M. Wilmot, O. Gozani and D. J. Patel, *Genes Dev.*, 2014, **28**, 1758–1771.

237 C. Yi, B. Chen, B. Qi, W. Zhang, G. Jia, L. Zhang, C. J. Li, A. R. Dinner, C.-G. Yang and C. He, *Nat. Struct. Mol. Biol.*, 2012, **19**, 671–676.